Hydrothermal fault zones in the lower oceanic crust: An example from Wadi Gideah, Samail ophiolite, Oman

Barbara Zihlmann[1)], Samuel Müller[2)], Rosalind M. Coggon[1)], Jürgen Koepke[3)], Dieter Garbe-Schönberg[2)], Damon A.H. Teagle[1)]

1) *Ocean and Earth Science, National Oceanography Centre Southampton, University of Southampton, Southampton, SO14-3ZH, UK*
2) *Institut für Geowissenschaften, Christian-Albrechts-Universität zu Kiel, Kiel, Germany*
3) *Institut für Mineralogie, Leibniz Universtität Hannover, Hannover, Germany*

Highlights

- Petrographic, major- and trace element and Sr-isotope characterization of a hydrothermal fault zone in the lower gabbroic crust, Samail ophiolite Oman.
- Mass balance calculations show significant losses of Si, Ca, Al, Rb, Sr and gains of H_2O, Cu, Zn, Ba and U during hydrothermal alteration.
- Silica solubility considerations indicate high fluid/rock ratios up to 450:1 – 900:1.
- Fault zone is a fossilized discharge zone of upwelling hydrothermal fluids in the deep plutonic rocks of ancient fast spreading ocean crust.
- Mass changes extrapolated to global elemental fluxes indicate that a lower crustal fault zone contributes significantly to the global hydrothermal budget of Si, Ti, Al, Fe, Mn, Mg, Ca, H2O, Cu, Zn, Sr and Cs.

Key words: ocean crust, layered gabbro, hydrothermal alteration, mass changes, global chemical flux, faults, Oman ophiolite

Abstract

Hydrothermal circulation is a key process for chemical and isotopic exchange between the solid Earth and oceans, and for the extraction of heat from newly accreted crust at mid-ocean

ridges. However, due to a dearth of samples from intact oceanic crust, or continuous sample suites from ophiolites, there remain major shortcomings in our understanding of hydrothermal circulation in the oceanic crust, especially in the lower plutonic crust. In particular, it remains unknown whether fluid recharge and discharge occurs pervasively or if it is mainly channelled within discrete zones such as faults.

Here, we describe a hydrothermally-altered fault zone that crops out in the Wadi Gideah in the layered gabbro section of the Samail ophiolite of Oman. A one metre thick normal fault comprising deformed chlorite ± epidote fault rock with disseminated chalcopyrite and pyrite, offsets gently dipping layered olivine gabbros. The chlorite-rich fault rocks surround strongly altered clasts of layered gabbro, 50 to 80 cm in size. Layered gabbros in the hanging wall and the footwall are partially altered and abundantly veined by epidote, prehnite, laumontite and calcite veins. In the wall rocks, igneous plagioclase ($An_{82\pm2\%}$) is partially altered towards more albitic compositions ($An_{75\text{-}81}$), and chlorite + tremolite partially replaces plagioclase and clinopyroxene. Clinopyroxene is moderately overgrown by Mg-hornblende.

Whole rock mass change calculations show that the chlorite-rich fault rocks are enriched in Fe, Mn, H_2O+CO_2, Co, Cu, Zn, Ba, and U, but have lost significant amounts of Si, Ca, Na, Cr, Ni, Rb, Sr, Cs, light rare earth elements (LREE), Eu, and Pb. Gabbro clasts within the fault zone as well as altered rock from the immediate hanging wall show enrichments in Na, volatiles, Sr, Ba and U and depletions of Si, Ti, Al, Fe, Mn, Mg, Ca, Cu, Zn, Rb, Cs, LREE, and Pb. Chlorite thermometry suggests a formation temperature of 300-350 °C for the fault rock and based on the Si loss and solubility of silica in hydrothermal fluids the intensity of alteration requires a fluid to rock ratio of up to 900:1. Strontium isotope whole rock data of the fault rock yield $^{87}Sr/^{86}Sr$ ratios of 0.7043-0.7048, which is considerably more radiogenic than fresh layered gabbro from this locality ($^{87}Sr/^{86}Sr$ = 0.7030 – 0.7033), and similar to black smoker hydrothermal signatures based on epidote, measured from epidote veins in the footwall and elsewhere in the ophiolite ($^{87}Sr/^{86}Sr$ = 0.7043-0.7051). Altered gabbro clasts within the fault zone show similar values with $^{87}Sr/^{86}Sr$ ratios of ~ 0.7045 – 0.7050. In contrast, the hanging and footwall gabbros display values only slightly more radiogenic than

fresh layered gabbro. The elevated strontium isotope composition of the fault rock and clasts together with the observed secondary mineral assemblages and calculated mass changes strongly supports the intense interaction with seawater-derived up-welling hydrothermal fluids, active during oceanic spreading. Assuming that such a fault zone is globally representative of faulting in the lower crust, an extrapolation of our results from mass change calculations to elemental fluxes, shows a significant contribution to the global hydrothermal budgets of Si, Ti, Fe, Mn, Mg, Ca, H_2O, Cu, Zn, Sr and Cs.

1. Introduction

Hydrothermal circulation throughout the oceanic crust is a fundamental process resulting in the exchange of chemical elements between the oceans and the solid Earth (Palmer and Edmond, 1989) as well as for extraction of heat from newly formed crust at mid-ocean ridges (Morton and Sleep, 1985; Sleep, 1991). Shallow hydrothermal fluid flow permeating the upper part of the oceanic crust is widely accepted for playing a vital role in cooling young crust at mid-ocean ridges. However, to date there remain major shortcomings in our understanding of the geometry and intensity of the deep circulation of seawater-derived hydrothermal fluids extending into the lower plutonic rocks of the ocean crust. In particular, the effectiveness of hydrothermal circulation in removing latent heat from the crystallizing magmas is not clear. There remain two, now long-standing, end-member conceptual models of how oceanic crust is accreted: The gabbro glacier model (e.g. Henstock et al., 1993; Morgan and Chen, 1993; Quick and Denlinger, 1993) and the sheeted sills model (e.g. Kelemen et al., 1997; MacLeod and Yaouancq, 2000), although hybrid models are also proposed (e.g. Boudier et al., 1996). The gabbro glacier model proposes the cooling of magma exclusively in a shallow melt lens and the formation of the lower crust by subsidence and downward flow of a crystal mush. In contrast, the sheeted sills model requires that substantial hydrothermal heat extraction occurs deep within the plutonic crust to remove latent heat and allow in-situ crystallization. Thermal models (Chen, 2001; Maclennan et al.,

2004; Theissen-Krah et al., 2016) suggest a mix between both end-member models is most likely but the proportion of crust crystallizing in-situ remains unclear. Cooling rate estimates derived from studies of Ca diffusion in olivine in the lower crust of the Samail ophiolite yield contrasting results as to whether the crust was cooled purely conductively or via hydrothermal circulation. Although data presented by Coogan et al. (2002) favours near conductive cooling, VanTongeren et al. (2008) suggest that hydrothermal circulation is likely to have extended to the base of the crust. Near conductive cooling in the upper plutonic section of the East Pacific Rise was also inferred from rate estimates based upon Mg in plagioclase (Faak et al., 2015) and from a combined Mg in plagioclase and Ca in olivine cooling rate study of gabbros from Hess Deep (Faak and Gillis, 2016). However, Mg and REE bulk diffusion between co-existing plagioclase and pyroxene in gabbros from the East Pacific Rise and Hess Deep (Sun and Lissenberg 2018) and coupled thermal modelling (Hasenclever et al., 2014) strongly support deep hydrothermal circulation. Due to insufficient observations of intact lower ocean crust it is poorly refined whether the circulation and cooling occurs via pervasive fluid flow along grain boundaries and vein networks or is focussed along major structures such as faults. Millimetre-scale amphibole vein networks are common in the lower gabbros of the ocean crust, and formed at near magmatic temperatures (Bosch et al., 2004; Coogan et al., 2007; Manning et al., 2000, 1996; Nicolas et al., 2003) but it is not clear if these features provide sufficient permeability to allow vigorous enough hydrothermal circulation to extract significant heat (Coogan et al., 2007; Manning et al., 2000, 1996). An alternative mechanism is to remove heat from the lower crust via more discrete, widely spaced regions of focussed fluid flow and discontinuous zones that preserve hydrothermal assemblages of high-temperature (~880 °C) to lower greenschist facies (< 300 °C) alteration, observed every ~1 km throughout the crust in the Samail ophiolite in Oman. Enhanced cooling rates are indicated in the surrounding crust of such focussed fluid flow zones (Coogan et al. 2006).

Here we present detailed field, petrographic and geochemical observations of a hydrothermal fault zone located within the lower layered gabbro section of the Samail ophiolite in Oman,

approximately 6 km below the paleo-seafloor and 1 km above the Moho transition zone (MTZ). We document the characteristics of a hydrothermal system deep in the crust which is so far only known from shallow hydrothermal environments and show that this fault provided a pathway for focussed hydrothermal discharge, giving evidence that hydrothermal activity was effective in mining heat from the plutonic section. Our primary aim of this study is to discuss the nature of the hydrothermal environment and to quantify elemental changes occurring within the fault zone itself and the alteration halo during intense hydrothermal alteration. Finally, we provide first estimates on the contribution of such a fault zone to the global chemical cycle.

2. Geological Overview

2.1. The Samail ophiolite

Fig. 1

The Samail ophiolite is regarded as the best analogue of fast-spreading oceanic crust preserved on land (e.g. Nicolas et al., 2000), and stretches approximately 550 km in length and 50 km in width along the coast of the Sultanate of Oman and the United Arab Emirates (UAE). The ophiolite is divided into several massifs (Fig. 1) and shows the complete "Penrose" sequence of rock types expected to be formed at a fast spreading mid-ocean ridge, from extrusive lavas, sheeted dikes, gabbros, layered gabbros and cumulate ultramafic rocks through the crust-mantle transition zone into the mantle sequence comprising harzburgite and locally dunite.

The ophiolite was formed in a spreading centre in the Neotethyan ocean during the Late Cretaceous (Searle and Cox, 1999). Late stage intrusive plagiogranitic bodies within the gabbro section yield ages of 97 to 93 Ma (Rioux et al., 2013) and mark the formation age of the crustal rocks within the ophiolite. There remains ongoing debate as to whether the Samail ophiolite formed at a mid-ocean ridge (MOR) in a major ocean basin or some form of

supra-subduction zone setting (SSZ; e.g., Alabaster et al., 1982; Boudier and Nicolas, 2007; Warren et al., 2007, 2005). Most evidence points to the partial influence of a subduction zone (e.g. Godard et al., 2003; Goodenough et al., 2014; Koepke et al., 2009; MacLeod et al., 2013). Although not completely absent, there is general consensus that the subduction zone influence is less pronounced in the southern part of the Samail ophiolite. Consequently, the lower crustal rocks exposed in the Wadi Tayin block of the ophiolite are an ideal location to investigate processes that occur during the accretion of the lower crust at fast spreading mid-ocean ridges.

2.2. The fault zone outcrop in Wadi Gideah

Fig. 2

The studied fault zone is located in Wadi Gideah (22.894 °N, 58.516 °E), about 15 km north of Ibra, in the crustal section of the Wadi Tayin massif. Wadi Gideah is situated to the west of Wadi Qafifah and Waid Khadir and to the east of Wadi Saq, Wadis where classic structural, petrographic and isotope geochemical observations on accretion of the crustal section of the ophiolite were made (Hopson et al., 1981; Pallister, 1981; Pallister and Knight, 1981), including oxygen- and strontium isotope studies (Gregory and Taylor, 1981; Lanphere et al., 1981). The north to south oriented Gideah valley cuts through a coherent series of lower oceanic crust and upper mantle rocks, exposing lithologies from the Moho transition zone up to the sheeted dike complex (Pallister and Hopson, 1981). Layered gabbros are the primary rock type and are exposed for ~6.5 km along the length of the valley. The magmatic layering of the gabbros dips ~28 ° to the south indicating a true thickness of ~3 km for the layered gabbro series. These rocks are overlain by foliated gabbros and isotropic high-level gabbros. Sheeted dikes are mostly eroded and are only exposed in small hills at the valley entrance and further out towards the Ibra syncline (Fig. 2). The Wadi Gideah area has been extensively sampled, and major rock types are well characterized in terms of their

petrographic and geochemical properties (France et al., 2009; Haase et al., 2016; Müller, 2016; Müller et al., 2017), including sulphur isotopes (Oeser et al., 2012).

Throughout the valley, from the layered gabbros up to the sheeted dikes, there are sub-vertical chlorite-rich zones, decimetres to metres-thick. They consist of dark green, weakly foliated, chlorite-rich rocks with the surrounding wall rock gabbros heavily altered for metres or up to tens of metres (Fig.2a). Field observations indicate that they occur every 1-2 km, either as isolated features or as part of a more extensively altered zone, similar to what has been described as a focussed fluid flow zone by Coogan et al. (2006). The zone investigated here consists of a chlorite-rich rock surrounded by heavily altered wall rock gabbro but in contrast to other observed zones it clearly crops out as a fault, making it unique. It is located within the layered gabbro section, approximately 1 km above the Moho transition zone (Fig. 2). A second fault zone is located about 40 metres to the east (Fig. 3a). Approximately 500 m towards south-east along strike of this fault zone outcrop, on the southern flank of a small ridge, partially to completely altered, gabbros crop out along the edge of the wadi terrace giving evidence for the continuity of this feature (Fig. 2b).

The fault zone is a normal fault, approximately one metre wide (Fig. 3b) and crops out over a length of eight metres. Its orientation of 251/55° (dip direction/dip) is sub-orthogonal to the magmatic layering (154/38°) nearby and sub-parallel to the mean strike of the sheeted dikes in this area (261/71°; Pallister, 1981), although dikes generally dip more steeply. The fault rock consists of a foliated Cu-sulphide-bearing dark greenish to blackish chlorite-rich rock that anastomoses around angular to lensoidal clasts (up to 50-80 cm) of altered gabbro. The hanging wall and footwall gabbros are altered and heavily veined by epidote, prehnite, laumontite and carbonate veins for 2.5 - 3 metres. The layered gabbro in the hanging wall is partially altered for ~30 m, manifested in a general bleaching of the rocks (Fig. 3b). A less intense halo extends only about 1 m into the footwall. Representative samples of the fault-rocks, clasts and surrounding altered wall rocks were collected during fieldwork in 2015 and

2016. These samples are compared with relatively fresh layered gabbro samples, collected < 500 m distance of the outcrop (Fig. 2b; Mueller et al., 2017).

Fig. 3

3. Analytical techniques

Polished thin sections were prepared from all samples. Minerals were identified using optical microscopy as well as a Carl Zeiss Leo1450VP Scanning Electron Microscope (SEM), at the University of Southampton, equipped with an Oxford Instruments EDS detector coupled to the Aztec Energy software system. Major element compositions of most minerals were analysed by electron probe microanalysis (EPMA) at the University of Kiel using a JEOL JXA 8900 R EMP operating at 15kV accelerating voltage and a focused and static 15nA beam current, applying 15 s counting times. Typical spot sizes were 2 µm except for plagioclase where the beam was defocused to ~5 µm. Compositions of chlorite, epidote and, sulphides in the chlorite-rich fault rock were measured at the Leibniz University in Hannover in Germany using a Cameca SX100 EMPA equipped with five spectrometers and Peak Sight software with a 15 kV focussed and static beam of 15 nA and 10 s counting times.

Whole rock samples were prepared for geochemical analysis at the University of Southampton. Samples were cut with a diamond saw to remove weathering rinds and prominent mineral veins, and saw marks were ground off with a high-speed diamond grinder. Samples were washed in Milli-Q water and ultrasonicated multiple times and dried at 60 °C overnight. Each sample was crushed into < 5 mm chips between a plastic chopping board and sheets of clean paper in a hardened iron fly press, and powdered using a chrome-steel ring mill in a Rocklabs^{TM} bench-top grinder.

Major and trace element (V, Cr, Co, Ni, Cu, Zn, Rb, Sr, Y, Zr, Nb, Cs, Ba, La and Ce) concentrations were analysed by X-ray fluorescence (XRF) using a Spectro XEPOS_HE Energy Dispersive Polarised X-ray Fluorescence (EDPXRF) Analyser at the University of St. Andrews, following the procedure outlined in Toy et al. (2017). Precision and accuracy were better than ±2.5 % RSD and ± 5% RMSD for major elements and ± 5% RSD, ± 4 % RMSD

for most trace elements respectively (Table A1). Four samples were analysed at the University of Hamburg, using a PanAnalytical MagixPro X-ray fluorescence spectrometer and following the procedure of Vogel and Kuipers (1987).

Samples for trace element and strontium isotope analysis were processed in a Class 100 Clean Laboratory suite of the Geochemistry Research Group of the University of Southampton. 50 mg of rock powder was dissolved using a standard HF-HNO_3 digestion (for details see Harris et al., 2015). Trace element concentrations were measured by Inductively Coupled Plasma Mass-Spectrometry (ICP-MS) at the University of Southampton using a Thermo X-series II ICP-MS. Precision and accuracy were better than ± 5% RSD and ± 4% RMSD respectively for the majority of the elements (Table A1).

Major and trace elements of four fault zone samples and the eight background gabbros (Table A2) were analysed at Kiel University. For liquid analysis 250 mg of dried powder (105°C) was dissolved in perfluoroalkoxy (PFA) vials applying a multi-acid digestion protocol. All acids were sub-boiled and, all work was carried out under Class 100 clean laboratory conditions. Procedural blanks, duplicates, and international reference materials were processed the same way (for details see Garbe-Schönberg, 1993). Reproducibility of this digestion procedure is typically better than 1 %RSD (1SD). Major elements were analysed using a Spectro CIROS SOP ICP-OES. SiO_2 cannot be analysed after digestion procedures including hydrofluoric acid and were therefore calculated to 100% oxides with due regard to loss on ignition. Analytical precision was found to be better than 0.5-1 %. Matrix-matched calibration was done by solutions of certified reference materials basalt BHVO-2, basalt BE-N, and granite AC-E processed the same way as the samples. Accuracy was monitored with running digested solutions of basalt BIR-1 and gabbro JGb-2. Minor and trace element mass fractions were determined using an AGILENT 7500cs with (Be, In, Re) internal standardisation. The analytical precision is typically better than 0.5-2 %RSD (1SD) for all elements analyzed. Results for reference materials BHVO-2 and JGb-1 are reported in Table A1.

Bulk composition of the aforementioned samples was also determined by LA-ICP-MS after

246 regrinding the samples and pressing into nano-particulate pressed powder pellets (NPP). A
247 193 nm ArF excimer laser ablation system (GeoLasPro, Coherent) coupled to an Agilent
248 7500s ICP-MS was used here. The advantage of this approach is the full recovery of HFSE
249 composition from gabbros containing accessory minerals (zircon, spinel). Details of this
250 procedure can be found in Garbe-Schönberg and Müller (2014). Initial calibration was done
251 against NIST SRM612 using Ca as an internal standard. For applying a matrix-matched
252 correction BHVO-2, BIR-1 and JGb-1 were prepared the same way as the samples and
253 analysed in the same batch. Analytical precision is typically better than 1-5 %RSD (1SD) for
254 all elements analysed at concentrations > 10x LOD (Table A1).
255 All samples analysed at the University of Southampton for their strontium isotopic
256 composition were leached with 10% analytical grade acetic acid prior to digestion to remove
257 secondary calcium carbonate. Strontium was separated from dissolved samples using
258 Strontium spec^{TM} columns (for details see Harris et al., 2015) and analysed using a
259 ThermoFisher Scientific TritonPlus TIMS. Strontium standard NBS987 was measured as an
260 external standard. Throughout the analytical period the mean value of NBS987 (n=25) was
261 $^{87}Sr/^{86}Sr$ =0.710241 ± 0.000018 (2SD). Internal precision was monitored by measuring 150
262 ratios per sample and the error of each measurement is reported as the two standard error
263 (2SE).
264 Strontium isotope ratios of background gabbros were determined at the Institute of
265 Mineralogy of the Hannover University following Pin et al. (1994). The analyses were carried
266 out with a ThermoFinnigan Neptune MC-ICP-MS. International standards, used for precision
267 monitoring, were AMES, BIR-1, JGB-2, JMC, and NIST SRM 987. ^{86}Sr and ^{87}Sr were
268 corrected for ^{86}Kr and ^{87}Rb interferences and $^{87}Sr/^{86}Sr$ corrected for mass fractionation. The
269 mean value for $^{87}Sr/^{86}Sr$ in the external standard NBS987 was 0.710276 ±0.000012 (2SD).
270 All $^{87}Sr/^{86}Sr$ values were corrected to a NBS987 value of $^{87}Sr/^{86}Sr$=0.710248.

271

272 **4. Petrography**

4.1. Fresh layered gabbro

Eight samples of fresh layered gabbro within 500 m of the fault zone outcrop were taken to provide background reference samples (Table A2). These samples are a subset of a larger suite of rocks focussing on a reference section through the lower oceanic crust of fast-spreading ridges in the Wadi Gideah (Mueller et al., 2017). These olivine-bearing to olivine gabbros are fine to medium grained and consist of about 50% plagioclase, 40% clinopyroxene and 10% olivine. Orthopyroxene is absent. The original magmatic assemblage is mostly preserved although in some rocks hornblende and actinolite partially overgrow clinopyroxene. Primary oxides are rare. Igneous plagioclase is partially altered to more albitic compositions. Where clinopyroxenes are in contact with plagioclase, chlorite is developed along some grain boundaries and fractures, commonly with secondary oxides (Fig. 4a, b). Olivine is heavily fractured, serpentinised and partially forms iddingsite, but cores are mostly unaltered. Total alteration is typically less than 5 to 10%.

4.2. Footwall and hanging wall

Fig. 4

The footwall sample (OM15-3F) is relatively fresh compared to the other fault zone-related samples, showing alteration of 30 - 40%. The style of alteration is similar to that in the background gabbros. The formation of chlorite after plagioclase and clinopyroxene as well as actinolite + tremolite after clinopyroxene mostly occurs along grain boundaries. Fresh olivine is rare. Cores of clinopyroxenes are preserved although they are heavily traversed by a dense networks of fractures which is accompanied by secondary oxides and sub-microscopic alteration phases growing into fresh regions thereby attenuating the transparency. Plagioclase shows yellowish to light-brownish shading. A fracture related overprint is also present in plagioclase but this is not as strong as for clinopyroxene (Fig. 4c, d).

The alteration intensity for the two hanging wall samples (AH9, OM15-3A; Fig. 4e, f) ranges between 50 – 80 % with the initial magmatic texture and mineralogy being only partially preserved. Clinopyroxenes have a “rusty” appearance with corroded grain boundaries and abundant fractures and are commonly replaced by sub-micron to micron brown to green hornblende blades and tremolite/actinolite needles. More altered clinopyroxenes show coronas of chlorite ± tremolite when in contact with plagioclase. Plagioclases are more altered than clinopyroxenes, showing abundant fractures and partial replacement by fine-grained chlorite. Fresh olivine is absent. There are abundant veins in the hanging wall samples ranging from < 10 µm to 1 mm width. Prehnite and prehnite-laumontite veins cross-cut earlier alteration phases and are being cross-cut by later laumontite-calcite veins (Fig. 4e, f).

4.3. Clasts

The two clast samples (AH6, AH7) from the central part of the fault rock display variable degrees of alteration. Sample AH6 has a very similar alteration assemblage and intensity to the hanging wall samples but includes two (<1 mm) veinlets of brown hornblende, possibly formed during higher temperature (> 500 °C) hydrothermal alteration (Manning et al., 2000). Laumontite veins (<1 mm) cross-cut earlier alteration and are themselves cross-cut by later calcite veins. Late stage calcite also fills tiny open spaces between mineral grains, and appears to be the last alteration phase. In contrast, sample AH7 is almost completely altered with abundant calcite. Epidote partially replaces plagioclase and clinopyroxene. Clinopyroxene is mostly overgrown by green hornblende, actinolite/tremolite and chlorite. As a whole, the sample is brecciated and cemented by calcite, with prominent calcite veins (~ 1mm) cross-cutting earlier alteration phases and veins.

4.4. Chlorite-rich fault rock

Seven samples (AD5, AD6, AD7, DT-10, AH8, OM15-3C and OM15-3E) of the chlorite-fault rock have been analysed by thin section petrography. For all these samples the alteration intensity is close to 100%. The major constituents are chlorite (60 – 80 %), epidote (5 – 15 %), titanite (< 5%), chalcopyrite and pyrite (< 5 %) and native copper (< 5%). Moreover, most samples contain weathering products of sulphides such as iron-oxyhydroxides (5 – 10%), malachite (5%) as well as calcite (5 - 10 %). In mineralized samples layered, fine-grained, concentric zonations (Fig. 5a, b) with variable contents of SiO_2, CuO and FeO (Fig. 5c) are common. Sample DT-10 is dominated by weathering products and consists mainly of iron-hydroxides (65 %) and malachite (25 %) with chlorite (10 %) as a subordinate phase. Thin section petrography reveals the complete replacement of the original igneous minerals but a relict igneous texture is still visible (Fig. 5d). Radiating chlorite crystals (~ 250 µm) replace primary plagioclase and clinopyroxene and relict outlines of primary mineral grains remain visible in cross-polarized light. This indicates that the chloritised fault rocks are strongly altered gabbros rather than sheared hydrothermal veins. Commonly, chlorite coexists with fine-grained, granular titanite (<20 µm) and epidote crystals (~ 50 - 100 µm) (Fig. 5e). Most samples show patches (1 – 5 mm) dominated by epidote, with euhedral crystals (100 – 250 µm) grown into open-space (Fig. 5e) that is partially filled by chlorite or secondary calcite. Typically, open-space filling chlorites are inclusion-free, and not associated with titanite, suggesting that it may be precipitated directly from a hydrothermal fluid instead of replacing primary minerals. Although chalcopyrite and pyrite grains are now only very small (5 - 20 µm) and rare in most samples, the numerous areas (> 5 mm) with iron-hydroxides and malachite suggest they were previously abundant. Similar to the hanging wall, footwall and clast samples, calcite is the latest stage alteration mineral, mainly filling open spaces and thin veins that cross cut earlier alteration phases.

Fig. 5

5. Mineral chemistry

5.1 Plagioclase

Plagioclase from the hanging wall and footwall samples is compositionally similar to plagioclase from the layered gabbro section elsewhere in the Wadi Tayin area (Pallister and Hopson, 1981). Most footwall plagioclase yield anorthite compositions (An_{75-81}), slightly lower than the median composition of plagioclase in fresh layered gabbros ($An_{82\pm2\%}$) in Wadi Gideah (Fig. 6a; Table A3), but strongly albitised plagioclase are not present ($<An_{60}$). In contrast, plagioclase in the hanging wall rocks has very high anorthite contents ($>An_{90}$).
Fig. 6a

5.2 Amphibole

All measured amphiboles classify as Ca-amphiboles following the classification scheme of Leake et al. (1997) (Fig. 6b; Table A4) and compositions range from tremolite to actinolite, magnesiohornblende and tschermakite, with most analyses plotting in the tremolite-actinolite field. All analysed amphiboles show compositions similar to amphiboles observed elsewhere in the ophiolite`s gabbro section (Bosch et al., 2004) as well as in the plutonic section of modern oceanic crust (Alt et al., 2010). Amphiboles co-existing with chlorite in hanging and footwall samples have tremolite compositions with high Si and low Fe^{2+} abundances (Mg# >0.95). In contrast, amphiboles replacing clinopyroxenes in hanging wall sample OM15-3A mainly plot in the magnesiohornblende field with a few tschermakite compositions. All measured amphiboles display low Cl concentrations of < 0.05 wt. %.
Fig. 6b

5.3 Epidote

375 Epidote from the fault rock display a range of compositions with X_{Fe} (X_{Fe} =Fe/(Fe+Al))
376 ranging between 0.2-0.34 (Table A5). This is somewhat higher than previously reported from
377 epidote veins and epidote crystals in the alteration halos around hydrothermal veins in
378 gabbros from the lower crustal section of Wadi Haymiliya in the central part of the ophiolite
379 (X_{Fe} = 0 - 0.2 for most analysis; Nehlig and Juteau, 1988). Similar X_{Fe} compositions of epidote
380 with X_{Fe}=0.17-0.36 have been measured from the sheeted dikes and upper gabbros in
381 ODP/IODP Hole 1256D (Alt et al., 2010).

382

383 **5.4 Chlorite**

384 Chlorite is the most abundant mineral in the fault rocks and also a major secondary phase in
385 hanging wall and footwall samples. Chlorite replaces plagioclase and co-exists with tremolite
386 along grain boundaries between plagioclase and pyroxene crystals. This is similar to how it is
387 commonly observed in many ocean crustal rocks (e.g. Alt et al., 2010) as well as reported
388 from experiments of gabbroic rocks with seawater at temperatures between 300-475 °C
389 (Beermann et al., 2017). Both in hanging wall and footwall samples chlorite replacing
390 plagioclase and chlorite co-existing with tremolite display a narrow range in silica (5.3-6.1 Si
391 pfu), in contrast to chlorite from elsewhere in the ophiolite (France et al., 2009; Nehlig and
392 Juteau, 1988) and in modern oceanic crust (e.g. (Alt et al., 2010) (Fig. 6c). Chlorites from the
393 fault rocks yield a similar narrow range of silica but have considerably higher Fe/(Fe+Mg)
394 ratios of 0.38 to 0.56 than hanging wall and footwall samples, with some samples being iron-
395 rich, Fe/(Fe+Mg) > 0.55 (Fig. 6c; Table A6). Furthermore, chlorite from the hanging and
396 footwall gabbros have distinctive compositions too, with footwall chlorites Fe/(Fe+Mg) ratio at
397 0.23 to 0.3 being more iron-rich than hanging wall chlorites with Fe/(Fe+Mg) ratio from 0.18
398 to 0.22.
399 Fig. 6c

400

5.5 Prehnite and laumontite

Prehnite crystals from prehnite-laumontite veins have been analysed with the electron microprobe in the hanging wall sample OM15-3A (Table A7). Prehnite compositions are uniform with a calculated formula of $Ca_{1.98\text{-}2}Na_{0\text{-}0.02}(Al_{0.96\text{-}0.98}Fe_{0.01\text{-}0.02}^{3+})Al_{0.94\text{-}0.97}Si_{3.03\text{-}3.06}O_{10}(OH)_2$. Prehnite shows low iron concentrations with X_{Fe}=100*Fe ($Fe+Al^{iV}$) of 0.33-1.55. These results are comparable to the lowermost values reported by Nehlig and Juteau (1988) from late prehnite veins in the layered gabbro section of Wadi Haymiliya.

Laumontite in the prehnite-laumontite veins in hanging wall sample OM15-3A is homogeneous with low iron and sodium concentrations (Table A8). Calculated formula is $Ca_{3.38\text{-}3.91}Na_{0\text{-}0.15}K_{0.01\text{-}0.39}(Al_{7.51\text{-}7.81}Fe_{0\text{-}0.13}Si_{16.19\text{-}16.44})*18H_2O$.

6. Bulk rock major- and trace element compositions

Table 1

Fig. 7

6.1 Fresh layered gabbro

Eight samples of fresh layered gabbro that crop out within 500 m of the fault zone have compositions typical of mafic cumulates from Wadi Tayin area (Peucker-Ehrenbrink et al., 2012), the Samail ophiolite in general (Browning, 1984; Pallister and Hopson, 1981; Pallister and Knight, 1981) and modern fast-spreading ocean ridges (Gillis et al., 2014). These rocks have magnesium numbers [Mg# = 100 x $(Mg^{2+}/(Mg^{2+} + Fe^{Total})_{atomic}$] that cluster in a narrow range of Mg# = 88 to 90 and incompatible minor and trace element concentrations (e.g., K_2O, TiO_2, Zr, Y, Nb) are low to very low, demonstrating the gabbros primitive compositions (Fig. 7; Table 1). Loss on ignition (LOI) averages ~2 wt. %, indicating the presence of some minor alteration products. Chondrite-normalised rare earth element patterns show a depletion of the light rare earth element (LREE) and slightly decreasing abundance of the heavy rare earth elements (HREE). There is a strong positive Eu anomaly, reflecting the high

427 modal abundance of plagioclase in the samples (Fig. 8).

428 Fig. 8

429

430 **6.2 Hanging and footwall samples**

431 Relative to the unaltered layered gabbro, rocks from the hanging and the footwall have
432 comparable major element compositions, with only subtle variations (Fig. 7). One hanging
433 wall sample yields slightly lower values of CaO but still plots in the range of overall layered
434 gabbro samples of the Wadi Tayin area (Peucker-Ehrenbrink et al., 2012). All three samples
435 plot in the lower range of SiO_2 concentration. The hanging and footwall samples have higher
436 concentrations of volatiles with loss on ignition (LOI) of 7.4 wt. % on average, indicating that
437 they are more strongly altered than the fresh layered gabbro samples. Trace element
438 concentrations are not significantly different compared to fresh layered gabbro
439 concentrations (Fig. 7, Table 1), but tend to have slightly increased Sr concentrations and
440 generally lower concentrations of Cu. Chondrite-normalized rare earth element pattern are
441 identical to fresh layered gabbro (Fig. 8).

442

443 **6.3 Clast samples**

444 The two clast samples are slightly more variable in terms of major- and trace element
445 composition when compared to hanging and footwall samples. The highly altered sample
446 AH7 has clearly lower CaO and higher TiO_2 concentrations, similar to the chlorite fault rocks
447 (Fig. 7; Table 1). Both clast samples show slightly higher concentrations for Na_2O, possibly
448 reflecting the presence of more albitic plagioclase as well as elevated volatile contents with
449 LOI 5 wt. % and 14.5 wt. %. Concentrations of V, Co, Zn and Ni are comparable to those of
450 fresh olivine gabbro, whereas sample AH7 has a higher concentration for Cu. Rare earth
451 element patterns are very similar to fresh layered gabbro although with a less pronounced Eu
452 anomaly for the more altered sample AH7 (Fig. 8).

6.4 Chlorite-rich fault rocks

Major and trace element compositions of the chlorite-rich fault rock reflect the secondary mineral assemblage. All fault zone samples show high LOI values of 8-17 wt. %, resulting from the high abundance of hydrous minerals such as chlorite and epidote and weathering products (e.g., malachite and iron oxyhydroxides). The chlorite-fault rock samples show different and more variable major elemental compositions compared to fresh layered gabbro (Fig.7; Table 1). Total Fe_2O_3 is up to six times higher than in fresh samples, whereas CaO, SiO_2 and Na_2O concentrations are considerably lower. TiO_2 and MgO concentrations are slightly higher whereas Al_2O_3 appears unchanged. In terms of minor and trace elements, the concentrations of Cu, Co, Zn and V are strongly increased compared to fresh gabbros for some of the samples. Cu concentrations are very high for some of the samples, reflecting the presence of chalcopyrite and its weathering products such as malachite. Strontium concentrations are generally lower than in fresh samples, in parallel with lower CaO values. Rare earth elements concentrations and patterns show some differences compared to fresh layered gabbro samples (Fig. 8): All samples display no or negative Eu anomalies, compared to a positive anomaly in unaltered layered gabbro. This possibly reflects the disappearance of plagioclase. Furthermore, two samples yield significantly higher REE concentrations (up to 8x chondrite).

7. Strontium isotope compositions

Fig. 9

Strontium isotope bulk compositions of six fault rock samples, two clast samples, three hanging and footwall samples were determined and are compared to eight fresh layered gabbro samples collected within 500 m of the fault zone outcrop. Additionally, epidote from an epidote vein in the footwall, laumontite from a laumontite-calcite vein in the hanging wall,

and calcite from a calcite vein in the fault rock and from a calcite-laumontite vein in the hanging wall were mechanically separated by hand picking and analysed (Fig. 9; Table 1). Fresh layered gabbros display a relatively narrow range of Sr concentrations (100 – 150 µg/g) and isotope compositions ($^{87}Sr/^{86}Sr$ = 0.70299 – 0.70332). These Sr-ratios are slightly elevated compared to fresh MORB ($^{87}Sr/^{86}Sr$ = 0.70281) from modern oceanic crust (White et al., 1987) and some show slightly more radiogenic values compared to fresh layered gabbro elsewhere in the Samail ophiolite ($^{87}Sr/^{86}Sr$ ~ 0.70265-0.70320, McCulloch et al., 1980, Lanphere et al., 1981). The footwall sample plots with $^{87}Sr/^{86}Sr$ = 0.70327 close to fresh layered gabbro, indicating only very minor Sr isotopic exchange. In contrast, the hanging wall samples have more radiogenic values of $^{87}Sr/^{86}Sr$ = 0.70390-0.70475 compared to fresh layered gabbro ($^{87}Sr/^{86}Sr$ = 0.70299-0.70332), with sample OM15-3A also showing higher Sr concentration (221 µg/g) than fresh layered gabbro due to high abundance of hydrothermal laumontite and prehnite. The clast samples as well as the chlorite-rich fault rocks show a narrow range of strontium isotope composition ($^{87}Sr/^{86}Sr$ = 0.70451 – 0.70450), clearly shifted towards more radiogenic compositions, combined with low Sr concentrations compared to fresh layered gabbro (Sr=50-100 µg/g). These Sr-isotope ratios are similar to the range of hydrothermal epidote and amphiboles, and highly altered gabbros from the Wadi Tayin area (e.g., Bosch et al., 2004; Coogan et al., 2006). Moreover, epidote from a monomineralic epidote vein of the footwall shows very similar Sr-isotope composition ($^{87}Sr/^{86}Sr$ = 0.70428). These epidote grains have euhedral crystal habits and appear to have precipitated directly out of a hydrothermal fluid and therefore should directly reflect the Sr-isotopic composition of the fluid.

The separated laumontite of sub-millimetre thick veinlets, cross-cutting all other alteration stages yields Sr-isotope ratios ($^{87}Sr/^{86}Sr$ = 0.70737) close to 95 Ma-seawater (Fig. 9). Hand-picked calcite of laumontite-calcite veinlets display the most radiogenic values of $^{87}Sr/^{86}Sr$ = 0.70777 – 0.70823 and plot in the range of Cretaceous to Miocene sediments (Weyhenmeyer, 2000) and close to the strontium isotope composition of modern

groundwater ($^{87}Sr/^{86}Sr$ = 0.7078) from gabbro hosted wells in Wadi Tayin (pers. communication N. Bompard).

8. Discussion

8.1 Secondary mineralogy and hydrothermal fluid characteristics

Chlorite is a major constituent in both the fault rock as well as in hanging- and footwall gabbros and its composition can be used as a geothermometer to estimate alteration temperatures. Several studies report a systematic decrease of Si^{iV} coupled with an increase of Al^{iV} in chlorites with increasing temperature (Cathelineau, 1988; Cathelineau and Nieva, 1985; McDowell and Elders, 1980; Velde, 1991). This correlation was used by Cathelineau (1988) to develop an empirical geothermometer of general applicability in diagenetic, hydrothermal and metamorphic settings based on the incorporation of Al^{iV}. Several studies show that the Al^{IV}- temperature correlation is likely to be influenced by the Fe/(Fe+Mg) ratio of the chlorite (Jowett, 1991; Kranidiotis and MacLean, 1987) and the empirical geothermometer of Cathelineau (1988) was extended by a correction factor (Jowett, 1991). Using this adapted thermometer of Jowett (1991) we calculate temperatures of chlorite formation in the fault rock as well as chlorite in hanging wall and footwall (supplementary Fig. A9_3; Table A6). The majority of fault rock chlorites show formation temperatures between 300-350 °C (median temperature 330 °C), whereas hanging wall and footwall chlorite show a slightly larger spread of temperatures but most plot in the range of ~ 250-300 °C with a median temperature of 275 °C for footwall and 268 °C hanging wall chlorite (supplementary Fig. A9_3). Statistical analysis on the temperature range of all three lithology's show that the temperature difference between fault rock and both wall rocks are significant (see box plot in Fig. A9_3). However, petrographic observations indicate that chlorites of the fault and chlorites within the walls have formed at different conditions (e.g. different fluid/rock ratio, pH and time). Therefore, an additionally influence of the host rock composition on the chlorite formation temperature as stated by Xie et al. (1997) cannot be entirely ruled out (e.g. Fe_2O_3

content is very different between hanging- and footwall: ~5 wt% and fault rock: ~25 wt%; see Table 1). The difference in chlorite formation temperatures between the fault rock (~ 300-350 °C) and the hanging- and footwall (~ 250-300 °C) suggest an open system of multi-stage alteration and a fluid evolution towards a highly charged composition. The formation of chlorite in the hanging- and footwall during initial fluid migration along the fault at slightly lower temperatures (~ 250-300 °C), subsequent evolution and channeling of the hydrothermal fluids, accompanied by a temperature rise to 300-350 °C, re-equilibrating the chlorite along the fault but not the chlorite in the wall rocks, is a likely scenario.

The fault rock and clast samples have similar Sr-isotope compositions (Fig. 9) as the epidote vein in the footwall as well as epidote veins observed elsewhere in the ophiolite (e.g., Bosch et al., 2004; Coogan et al., 2006). The epidotes have relatively high Sr concentrations (400 to 750 μg/g) and are robust against low-temperature fluid-rock Sr exchange and hence analyses of epidote precipitated in veins are commonly used to estimate the Sr-isotopic compositions of the hydrothermal fluids (e.g., Bickle and Teagle, 1992; Harris et al., 2015; Teagle et al., 2003). Epidosites, equigranular epidote-quartz-titanite rocks, are present in the sheeted dike complexes of many ophiolites, and thought to record zones of concentrated "black smoker-type" hydrothermal upwelling fluid flow (e.g., Richardson et al., 1987; Schiffman et al., 1987) and have similar Sr-isotopic compositions to epidote veins. The Oman epidote $^{87}Sr/^{86}Sr$ ratios are clearly elevated relative to fresh layered gabbro indicating the extensive exchange of the rock with a seawater-derived hydrothermal fluid. We propose that this fluid had a $^{87}Sr/^{86}Sr$ in the range of 0.7043-0.7048, and that the passage of a black smoker-like fluid with this Sr-isotopic composition resulted in the alteration of the fault rocks, clasts and surrounding wall rocks.

The degree of alteration, the strontium isotopic composition of the fault rock and particularly the observed secondary mineral assemblage with abundant Cu-sulphides suggest a formation of the fault rock during fluid-rock interactions with up-welling, discharging

hydrothermal fluids at chlorite formation temperatures of about 300-350 °C. Hints towards enhanced fluid recharge activity are absent in this fault. Minor but pervasive replacement of clinopyroxene by Mg-hornblende in the altered clast and hanging wall samples indicates an earlier phase of higher temperature hydrothermal alteration which is now mostly overprinted by the described, lower-temperature alterations.

8.2 Mass changes during hydrothermal fluid-rock interaction

8.2.1 Calculating mass changes

Comparison of altered bulk rock composition with relatively fresh rocks allow us to estimate the effects of hydrothermal alteration more quantitatively. These calculations indicate which elements are either immobile, mobilized or precipitated, and ultimately lost or gained during fluid-rock interactions. To calculate net mass changes, it is essential that altered rocks are compared with appropriate precursor compositions. Widely available analyses for fresh Oman gabbros makes this simpler than in more complex or metamorphosed terranes. A widely applied method to monitor changes during hydrothermal alteration uses the behaviour of immobile elements that are passively concentrated or diluted by whole rock mass loss or mass gain, respectively (Grant, 1986; Gresens, 1967; MacLean, 1990; MacLean and Barrett, 1993). Therefore, concentration ratios of these immobile elements in the rock before and after alteration can be used to calculate changes of other, mobile elements. Grant (1986) re-defined the original equation of Gresens (1967), relating the concentration of an element *i* in the altered rock to the concentration of the same element in the precursor rock through a mass change term ($\frac{M^0}{M^A}$). The change of concentration of element *i* during alteration is the difference between the concentration of element *i* before (c_i^0) and after (c_i^A) alteration. The equation is formulated as:

$$c_i^A = \frac{M^0}{M^A} (c_i^0 + \Delta c_i) \quad (1)$$

where c_i^A = concentration of component *i* in the altered rock, c_i^0 = concentration of element *i* in the precursor rock, M^0 = mass of the precursor rock, M^A = mass of the altered rock and Δc_i = change in concentration of element *i*. This equation describes a straight line with a slope defined by the mass change term ($\frac{M^0}{M^A}$) and the y-axis intercept ($\frac{M^0}{M^A} * \Delta c_i$).

To calculate elemental gains and losses for each altered sample, precursor compositions need to be defined. In the case of the chlorite-rich fault rock within the layered gabbros presented here, a single precursor system is assumed, as the layered gabbros are chemically reasonably homogenous (Fig 7 & 8). For this study, the median concentrations of eight samples of the fresh layered gabbro within 500 m of the fault zone outcrop was taken as a precursor composition (Table A2). To select which elements can be considered as immobile and are, therefore, appropriate for calculating the mass change term, each of the seven samples from the chlorite-fault zone was examined individually, by comparing the concentration of element *i* in the altered rock (c_i^A) to the median value of the precursor rock (c_i^0). For all the fault-rock samples the c_i^A / c_i^0 for HREE cluster together (Fig. 10). Hence, we have selected the HREE (Dy and heavier) to calculate the mass change term ($\frac{M^0}{M^A}$).

Table 2

Fig. 10

8.2.2 Chemical changes during hydrothermal alteration

Results of mass change calculations are summarized in Table 2 and median mass changes are plotted in Fig. 10. Chlorite-rich fault rock samples show an average a significant mass loss of 67% and clast samples a loss of 34%. In contrast, there is no significant mass change (- 1%) for hanging and footwall samples. Major element changes are variable, both within and between the three rock types, mainly reflecting differences in the secondary mineral assemblages formed and the extent of fluid-rock exchange.

SiO_2 is slightly to highly reduced in all samples with increasing alteration (Fig. 10). Chlorite fault rock samples have lost >60 % of their silica compared to fresh layered gabbro. This is a

substantial part of the total mass loss calculated for chlorite-rich rocks. There is no altered gabbro sample showing any silica enrichment. This agrees well with the absence of secondary quartz and suggests that silica has been transported away from these rocks by the passage of hydrothermal fluids. The general silica loss due to hydrothermal alteration of oceanic crust has been described previously (e.g. Coggon et al., 2016). The behaviour of silica in hydrothermal fluids is relatively well understood (Von Damm et al. (1991), and the silica-loss (63%) from the chlorite-rich fault zones can be used to calculate how much fluid has flowed through this fault zone. The solubility of SiO_2 in hydrothermal fluids principally depends on temperature, pressure and salinity. Using the quartz solubility in seawater of 15.7 and 31.2 mmol/kg, at 300 and 400°C, respectively (Von Damm et al., 1991), results in fluid/rock ratios between 450:1 to 900:1. This estimation is possibly an upper limit as some mid-ocean ridge hydrothermal fluids have salinities greater than seawater, and quartz solubility increases with increasing salinity (Xie and Walther, 1993), but it assumes that the mobilisation of silica is 100% efficient. Regardless, the chlorite-rich fault rocks forms at extreme fluid/rock ratios (Teagle and Alt, 2004).

Titanium and aluminium are traditionally assumed to be immobile during hydrothermal alteration (e.g. MacLean and Barrett, 1993), but these elements display slight mobility in all three of the altered rock types. Titanium shows changes in the range of slightly more than ± 10% which is consistent with the formation of secondary titanite in the chlorite fault rock. Despite the localized formation of secondary titanite, the fault rocks have lost titanium compared to fresh layered gabbro (median= -14%). Alumina is slightly to moderately depleted. This loss of alumina may relate to the strong losses of calcium for all three rock types and a gain of sodium for hanging and footwall samples as well as clasts, due to the partial albitisation of plagioclase (Fig. 6 & 11). The chlorite-rich fault rocks have lost >90 % of calcium compared to fresh layered gabbro reflecting the complete breakdown of plagioclase, with only minor epidote present. Iron and manganese are moderately to highly depleted in hanging and footwall rocks and clasts respectively, whereas the chlorite-rich fault rocks are highly enriched in both elements (Fig. 10). The high iron concentrations mainly reflect

hydrothermal sulphide mineralisation and their subsequent iron oxyhydroxide weathering products, respectively.

The most significant feature of all three rock types is the large increase of volatiles, as seen in an increase of loss on ignition (LOI) when compared to fresh layered gabbro. This increase mainly reflects hydration during fluid-rock interaction with only minor carbonation. The hanging and footwall samples as well as clast sample AH6 have only minor calcium carbonates present in small veins. Consequently, most of the increase in LOI is due to the formation of hydrous hydrothermal minerals such as chlorite, amphibole, prehnite and laumontite. Hanging wall sample OM15-3A shows a considerable gain of volatiles, reflecting high modal abundances of laumontite and prehnite. For clast sample AH7 and all the fault rock samples the increase of LOI is mainly due to high abundances chlorite (± minor epidote).

Even though Y, Zr and Hf are generally considered as immobile elements during hydrothermal processes (MacLean and Barrett, 1993; MacLean and Kranidiotis, 1987), but they show considerable mass gains in all three rock types. However, fresh layered gabbros and altered samples have low concentrations of Zr (~ 3-15 μg/g) and Y (~ 4-13 μg/g), and consequently, minor variations in concentration can result in considerable relative mass gains or losses. However, mobility of high-field strength elements (HFSE) in hydrothermal systems and hydrothermal zircons have been reported from MOR settings (e.g. Augustin et al., 2008).

In general, the alkali elements are very sensitive tracers of hydrothermal activity. Lithium is depleted in all three rock types, up to 50% in hanging and footwall and clasts but slightly less so in the chlorite-rich fault rocks (Fig. 10). Lithium is known to be highly mobile during hydrothermal processes in oceanic crust: low-temperature processes lead to an increase in Li concentration in host rocks but, Li is significantly mobilised by hydrothermal processes at greenschist to sub-amphibolite facies conditions (Chan et al., 2002). Interestingly, Li is less depleted in the chlorite-rich fault rock compared to the other two rock types, despite the

666 higher alteration degree. This may be explained by the substitution of Li for Mg, due to their
667 similar ionic radii (~ 0.76 Å), and the high abundance of Mg-chlorite in these rocks. Both, Rb
668 and Cs are depleted in all three rock types (Fig. 10), suggesting they were leached and lost
669 to the hydrothermal fluid. From black smoker systems it is well known that Rb and Cs are
670 leached almost completely during intensive fluid-rock interaction at temperatures ~350 °C
671 leading to Rb and Cs concentrations of black smoker fluids nearly as high as measured in
672 basalts (Palmer and Edmond, 1989; Von Damm, 1995). Sr and Ba have an affinity for Ca,
673 and Sr is predominantly incorporated in secondary minerals such as secondary plagioclase,
674 prehnite and laumontite in hanging wall and footwall and is therefore gained. Even though Sr
675 substitutes for Ca of epidote in the fault rock, it cannot counterbalance the loss of Sr due to
676 the decay of plagioclase and therefore Sr is highly depleted in the fault rock. Ba is enriched
677 in both the wall samples and the clasts and slightly enriched in the fault rock, although the
678 range in the fault rock is large.

679 Sc, V, Cr, Ni and Pb are all depleted in hanging and footwall, clasts and the fault rock,
680 whereas Co, Cu and Zn are depleted in hanging and footwall but present in high
681 concentrations in the chlorite-rich fault rocks, reflecting sulphide mineralisation and their
682 weathering products (Fig. 10). Although clast sample AH6 shows similar behaviour to the
683 hanging and footwall samples, the more altered sample AH7 has elevated Cu and Zn
684 concentrations, reflecting the presence of sulphides. Mass change calculations indicate that
685 Co, Zn, and Cu are leached out of the precursor rock during intensive hydrothermal fluid-rock
686 interaction and precipitated locally in the fault rock. Presumably, this alteration occurred at
687 relatively high temperatures (~350 °C), where the solubility of metals in hydrothermal fluids is
688 significantly increased (Seewald and Seyfried, 1990). Such a metal depletion during
689 hydrothermal alteration has been observed in other oceanic and ophiolitic crustal sections,
690 from both the lower and the upper crust (Alt et al., 2010; Coggon et al., 2016; Coogan et al.,
691 2006; Heft et al., 2008; Humphris et al., 1998; Nehlig et al., 1994).

692 Fig. 10

693 For all three alteration types the behaviour of the LREE (La-Sm) is decoupled from the HREE
694 (Gd-Lu). The HREE have been assumed to be immobile and were used to normalize mass
695 changes. In contrast, the LREE are depleted in most samples when compared to fresh
696 layered gabbro, with La being most depleted. A pronounced negative Eu anomaly is common
697 to all altered rock types (Fig. 10) and is presumably related to both, albitisation of plagioclase
698 (Klinkhammer et al., 1994) and fluid chemistry coupled with specific pressure and T
699 conditions (Beermann et al., 2017). This is most extreme in the chlorite-rich fault rocks,
700 where plagioclase is completely dissolved and replaced, leading to a release of Eu into the
701 hydrothermal fluid. In contrast, there are three samples (AD5, AD7 and OM15-3E) that
702 display gains of LREE and a less pronounced negative Eu anomalies (supplementary Fig.
703 A9). This reflects the presence of open-space filling epidote in these samples that appear to
704 have precipitated directly from the hydrothermal fluid rather than as a replacement of primary
705 igneous minerals. Hydrothermal epidote tends to show flat to slightly LREE-enriched
706 patterns, with a pronounced positive Eu anomaly (Gillis et al., 1992).

707 U is generally highly enriched in all three rock types (Fig. 10) whereas it shows low
708 abundances in fresh layered gabbro. Previous studies from the upper oceanic crust have
709 shown that U is enriched during low-temperature (<100 °C) hydrothermal process (Bloch,
710 1980; Hart and Staudigel, 1982), although Bach et al. (2003) suggest that U uptake
711 continues under lower greenschist facies conditions. Ba is enriched in all three rock types,
712 indicating an uptake during hydrothermal alteration.

713

714 **8.3 The effect of weathering**

715 Some of the samples are not only affected by hydrothermal alteration but also show signs of
716 weathering (e.g. formation of oxyhydroxides, carbonates). Especially some of the fault rock
717 samples (DT-10 and OM15-3C) show high contents of CO_2 and H_2O-bearing weathering
718 minerals such as malachite and Fe-hydroxide. Such weathering minerals also contribute to
719 the high observed gain of volatiles. Moreover, Fe-oxyhydroxides are proposed to host or

adsorb U (Bach et al., 2003; Staudigel et al., 1996; Teagle et al., 1996), indicating that U uptake might extend to the surface weathering processes.

Additionally, calcite from laumontite-calcite veins shows the most radiogenic compositions, close to present day groundwater observed in gabbro hosted wells in Wadi Tayin and within the range of Miocene sediments that once covered the ophiolite. This indicates that calcite is likely to have formed later in the history of the ophiolite and is not necessarily related to the ocean ridge hydrothermal circulation and alteration previously described.

8.4 Importance of lower crustal fault zone for global elemental fluxes

To assess the hydrothermal contribution of fault zones similar to the feature described above to global geochemical cycles, we have converted our estimated hydrothermal mass changes to net elemental fluxes into or from the lower crust. Given our field observations and aerial photograph observations on the occurrence of these altered zones (Coogan et al., 2006), we assume that similar faults are spaced every 1000m perpendicular to the ridge axis and continue along strike for 500 m, such that there is one fault zone per square kilometre of seafloor. The modelled fault zones comprise 0.6 m of fault rock and 0.4 m of clasts, flanked by a of 30 m wide alteration halo (total width, including hanging wall and footwall) and cut through 4000 m of gabbro (Fig. 11). The net mass flux (F_i) of component *i* through 1 square kilometre of seafloor due to lower crustal faulting is therefore given by:

$$F_i = \sum_{z}^{FZ} V_z \rho_z \Delta m_{i-z}$$

Where $\Delta m_{i\text{-}z}$ is the average change in mass of component *i* per kilogram of rock in each sub-zone (z) of the fault zone (FZ), V_z is the volume of each sub-zone (fault rock = 1.2 x 10^6 m^3, clasts = 0.8 x 10^6 m^3, halo = 100 x 10^6 m^3) and ρ_z is the density of each sub-zone (assumed to be 3100, 2700 and 2800 kg/m^3, for the fault rock, clasts and halo respectively). Sources of uncertainty in the calculated values of F_i will include (i) geochemical analytical uncertainty; (ii)

745 uncertainty in calculated hydrothermal mass changes, for example reflecting the choice of
746 precursor composition, the assumptions regarding element immobility, and the compositional
747 variability within each altered sub-zone of the fault; and (iii) uncertainty in fault geometry and
748 spacing, and hence the modelled volumes of fault sub-zones (V_z). A full propagation of these
749 errors is beyond the scope of this paper. Here the net elemental mass fluxes (F_i) due to lower
750 crustal faulting are therefore determined from the median calculated chemical changes for
751 each sub-zone of the fault (see Section 8.2.2), with the uncertainty propagated from the
752 median absolute deviation of the calculated chemical changes for each rock type, as
753 compositional variability of the altered rocks is expected to be the dominant source of
754 uncertainty. The impact of uncertainty in fault geometry/spacing is discussed below.

755 To assess the importance of such fault zones to global hydrothermal budgets, we compare
756 our calculated hydrothermal fluxes due to lower crustal faulting with published estimates of
757 the hydrothermal fluxes associated with the pervasive 'background' alteration of ocean crust
758 determined from analyses of: (i) a full section of 10 Ma ocean crust sub-aerially exposed in
759 the sub-Antarctic Maquarie Island ophiolite; and (ii) samples of ocean crust recovered from
760 several sites by scientific ocean drilling, that were combined to yield a composite full-crustal
761 section (Staudigel, 2014; Table 3). The 2.7 km thick Macquarie crustal section includes
762 lavas, a mineralised lava-dike transition zone, sheeted dikes, and 1 km of lower crustal
763 gabbros produced at a slow spreading rate (10 mm/y half rate). The hydrothermal fluxes of
764 the composite section were predominantly determined from analyses of 120 Ma slow-spread
765 lavas and 9 Ma ultra-slow spread gabbros. Note that there are significant discrepancies
766 between the results of these two studies, which likely reflect both global variations in the
767 nature and extent of hydrothermal alteration and the differing methods used to calculate the
768 hydrothermal fluxes (see discussion in Coggon et al., 2016). Here we consider lower crustal
769 hydrothermal faulting to make a significant contribution to global hydrothermal budgets for a
770 given element if the magnitude of our calculated flux is >10% of the hydrothermal flux in to or
771 from either the Macquarie crust or the composite crustal section (Table 3). Our results
772 indicate that given our assumed fault spacing and geometry, lower crustal faults contribute

773 significantly to the global hydrothermal budgets of Si, Ti, Al, Fe, Mn, Mg, Ca, H_2O, Cu, Zn, Sr
774 and Cs (Fig. 12).

775 Assuming that hydration is the main cause of volatile enrichment within the sampled fault
776 zones, our results indicate that the previously undocumented additional water-uptake during
777 lower crustal faulting is equivalent to 20% of the total water uptake during background
778 alteration of ocean crust (Coggon et al., 2016; Staudigel, 2014).
779 For elements such as Ca, Al, Fe, Na, Zn and Sr, where the change (compared to Macquarie
780 crust) is in the same sense, our results clearly indicate a significant previously unquantified
781 flux. For other elements such as Si or Cu, where the change is not the same sense and
782 elements previously were assumed to leave the crust, it may be that they be partially
783 remobilized into the fault zones.

784 Here we have shown that if the lower crustal faulting observed within the Semail ophiolite is
785 globally representative of faulting within lower ocean crust, then such fault zones contribute
786 significantly to the global hydrothermal budgets for many elements. Furthermore, if we have
787 underestimated the spacing of lower crustal fault zones [e.g. fault spacing of only a few
788 hundred metres observed at the East Pacific Rise (Bicknell et al., 1987; Bohnenstiehl and
789 Carbotte, 2001; Edwards et al., 1991)], and/or the width of the fault zone alteration halo (the
790 dominant mass-fraction of the fault zone), then their contribution to global hydrothermal
791 fluxes is even more significant.

792

793 **9. Conclusions**

794 Secondary mineral assemblages, major- and trace element mass change calculations and
795 strontium isotope compositions suggest that this chlorite-rich fault zone represents a
796 fossilized discharge zone of hot, upwelling hydrothermal fluids with Sr-isotopic compositions
797 in the range $^{87}Sr/^{86}Sr$ = 0.7043-0.7048, similar to epidote present in hydrothermal veins in the
798 Samail ophiolite. Chlorite thermometry indicates formation temperatures of 300-350 °C for

799 the fault rock and calculations based on silica solubility in hydrothermal fluids give an
800 estimate of high fluid/rock ratios up to 450-900. Due to intensive fluid-rock interaction
801 elements were mobilized and locally redistributed. Ca, Na, Si, Al, Mg, Mn, Fe, Ti as well as
802 Pb, Rb, Cs, Cr, N, Sc, V, Cu, LREE, Co, Zn and Li were leached and either transported away
803 by the passage of hydrothermal fluids or were partially incorporated into secondary phases
804 such as chalcopyrite and pyrite (Fe, Cu, Zn, Co) or epidote (LREE) in the fault rock itself or
805 into secondary phases such as plagioclase, prehnite and laumontite (Na, Sr) in the wall
806 rocks. H_2O and other elements such as Ba, U were transported with the hydrothermal fluid
807 and scavenged within the system. Exchange of the hydrothermal fluid with the rock is limited
808 to between 1 and 30 metres from the fault zone, as evidenced by the alteration around the
809 fault zone observed in the field. Our results suggest that hydrothermal fluids reach deep into
810 the lower plutonic oceanic crust and, hence, provide an efficient cooling system being the
811 prerequisite for in situ crystallization and accretion as proposed in the sheeted sills model.
812 From calculated mass changes we estimated global hydrothermal fluxes for one lower
813 crustal fault zone per one cube of lower oceanic crust (1 km x 1 km x 4 km), assuming a
814 crustal production rate of 5 km^2/y. Our results indicate that given the assumed fault spacing
815 and geometry, lower crustal faults contribute significantly to the global hydrothermal budgets
816 of Si, Ti, Al, Fe, Mn, Mg, Ca, H_2O, Cu, Zn, Sr and Cs.
817

818 **Acknowledgements**

819 We greatly acknowledge reviews from A. Barker and an anonymous reviewer that helped to
820 improve this manuscript. T. Müller is thanked for providing $^{87}Sr/^{86}Sr$ measurements of eight
821 fresh layered gabbro samples. We thank M. Cooper, U. Westernströer, and K. Bremer for
822 their assistance in the laboratories, A. Barker and L. Crispini for helpful thin section
823 discussions, M. Schori and O. Beermann for fieldwork assistance and M. Harris for providing
824 figure 11. We thank the Public Authority for Mining of the Sultanate of Oman for allowing us
825 to conduct field work. The research leading to these results received funding from the People

826 Programme (Marie Curie Actions) of the European Union`s Seventh Framework Programme
827 FP7/2007-2013 under the REA grant agreement n°608001, that supported BZ within the
828 “Abyss” Initial Training Network. DT is supported by a Royal Society Wolfson Research Merit
829 Award (WM130051). Further essential funding was contributed to DGS under DFG research
830 grant GA 1960/11-1.
831
832
833
834
835

836 **References**

837 Alabaster, T., Pearce, J.A., Malpas, J., 1982. The volcanic stratigraphy and petrogenesis of
838 the Oman ophiolite complex. Contributions to Mineralogy and Petrology 81, 168–183.

839 Alt, J.C., Laverne, C., Coggon, R.M., Teagle, D.A.H., Banerjee, N.R., Morgan, S., Smith-
840 Duque, C.E., Harris, M., Galli, L., 2010. Subsurface structure of a submarine
841 hydrothermal system in ocean crust formed at the East Pacific Rise, ODP/IODP Site
842 1256. Geochemistry, Geophysics, Geosystems 11, 1–28. doi:10.1029/2010GC003144

843 Augustin, N., Lackschewitz, K.S., Kuhn, T., Devey, C.W., 2008. Mineralogical and chemical
844 mass changes in mafic and ultramafic rocks from the Logatchev hydrothermal field
845 (MAR 15 N). Marine Geology 256, 18–29.

846 Bach, W., Bernhard, P.E., Hart, S.R., Blusztajn, J.S., 2003. Geochemistry of hydrothermally
847 altered oceanic crust: DSDP/ODP Hole 504B-Implications for seawater-crust exchange
848 budgets and Sr-and Pb-isotopic evolution of the mantle. Geochemistry, Geophysics,
849 Geosystems 4, 40–55. doi:10.1029/2002GC000419

850 Beermann, O., Garbe-Schönberg, D., Bach, W., Holzheid, A., 2017. Time-resolved
851 interaction of seawater with gabbro: An experimental study of rare-earth element
852 behavior up to 475° C, 100 MPa. Geochimica et Cosmochimica Acta 197, 167–192.

853 Bickle, M.J., Teagle, D.A.H., 1992. Strontium alteration in the Troodos ophiolite: implications
854 for fluid fluxes and geochemical transport in mid-ocean ridge hydrothermal systems.
855 Earth and Planetary Science Letters 113, 219–237.

856 Bicknell, J.D., Sempere, J.-C., Macdonald, K.C., Fox, P.J., 1987. Tectonics of a fast
857 spreading center: A Deep-Tow and Sea Beam survey on the East Pacific Rise at 19 30′
858 S. Marine Geophysical Researches 9, 25–45.

859 Bloch, S., 1980. Some factors controlling the concentration of uranium in the world ocean.
860 Geochimica et Cosmochimica Acta 44, 373–377.

861 Bohnenstiehl, D.R., Carbotte, S.M., 2001. Faulting patterns near 19 30′ S on the East Pacific
862 Rise: Fault formation and growth at a superfast spreading center. Geochemistry,
863 Geophysics, Geosystems 2.

864 Bosch, D., Jamais, M., Boudier, F., Nicolas, A., Dautria, J.M., Agrinier, P., 2004. Deep and
865 high-temperature hydrothermal circulation in the Oman ophiolite - Petrological and
866 isotopic evidence. Journal of Petrology 45, 1181–1208.

867 Boudier, F., Nicolas, A., 2007. Comment on “dating the geologic history of Oman’s Semail
868 ophiolite: Insights from U-Pb geochronology” by C. J. Warren, R. R. Parrish, D. J.
869 Waters and M. P. Searle. Contributions to Mineralogy and Petrology 154, 111–113.
870 doi:10.1007/s00410-007-0189-5

871 Boudier, F., Nicolas, A., Ildefonse, B., 1996. Magma chambers in the Oman ophiolite: fed
872 from the top and the bottom. Earth and Planetary Science Letters 144, 239–250.

873 Browning, P., 1984. Cryptic variation within the cumulate sequence of the Oman ophiolite:
874 magma chamber depth and petrological implications. Geological Society, London,
875 Special Publications 13, 71–82.

876 Cathelineau, M., 1988. Cation site occupancy in chlorites and illites as function of
877 temperature. Clay minerals 23, 471–485.

878 Cathelineau, M., Nieva, D., 1985. A chlorite solid solution geothermometre. The Los Azufrez
879 (Mexico) geothermal system. Contributions to Mineralogy and Petrology 91, 235–244.

880 Chan, L.H., Alt, J.C., Teagle, D.A.H., 2002. Lithium and lithium isotope profiles through the
881 upper oceanic crust: A study of seawater-basalt exchange at ODP Sites 504B and
882 896A. Earth and Planetary Science Letters 201, 187–201. doi:10.1016/S0012-
883 821X(02)00707-0

884 Chen, Y.J., 2001. Thermal effects of gabbro accretion from a deeper second melt lens at the
885 fast spreading East Pacific Rise. Journal of Geophysical Research: Solid Earth 106,

886 8581–8588.

887 Coggon, R.M., Teagle, D.A.H., Harris, M., Davidson, G.J., Alt, J.C., Brewer, T.S., 2016.
888 Hydrothermal contributions to global biogeochemical cycles: Insights from the
889 Macquarie Island ophiolite. Lithos 264, 329–347.

890 Coogan, L.A., Howard, K.A., Gillis, K.M., Bickle, M.J., Chapman, H., Boyce, A.J., Jenkin,
891 G.R.T., Wilson, R.N., 2006. Chemical and thermal constraints on focussed fluid flow in
892 the lower oceanic crust. American Journal of Science 306, 389–427.

893 Coogan, L.A., Jenkin, G.R.T., Wilson, R.N., 2002. Constraining the cooling rate of the lower
894 oceanic crust: a new approach applied to the Oman ophiolite. Earth and Planetary
895 Science Letters 199, 127–146.

896 Coogan, L.A., Manning, C.E., Wilson, R.N., 2007. Oxygen isotope evidence for short-lived
897 high-temperature fluid flow in the lower oceanic crust at fast-spreading ridges. Earth and
898 Planetary Science Letters 260, 524–536.

899 Edwards, M.H., Fornari, D.J., Malinverno, A., Ryan, W.B.F., Madsen, J., 1991. The regional
900 tectonic fabric of the East Pacific Rise from 12 50′ N to 15 10′ N. Journal of Geophysical
901 Research: Solid Earth 96, 7995–8017.

902 Faak, K., Coogan, L.A., Chakraborty, S., 2015. Near conductive cooling rates in the upper-
903 plutonic section of crust formed at the East Pacific Rise. Earth and Planetary Science
904 Letters 423, 36–47.

905 Faak, K., Gillis, K.M., 2016. Slow cooling of the lowermost oceanic crust at the fast-spreading
906 East Pacific Rise. Geology 44, 115–118.

907 France, L., Ildefonse, B., Koepke, J., 2009. Interactions between magma and hydrothermal
908 system in Oman ophiolite and in IODP Hole 1256D: Fossilization of a dynamic melt lens
909 at fast spreading ridges. Geochemistry, Geophysics, Geosystems 10, 1–30.
910 doi:10.1029/2009GC002652

911 Garbe-Schönberg, C.D., 1993. Simultaneous determination of thirty- seven trace elements in
912 twenty- eight international rock standards by ICP- MS. Geostandards Newsletter 17,
913 81–97.

914 Garbe-Schönberg, D., Müller, S., 2014. Nano-particulate pressed powder tablets for LA-ICP-
915 MS. Journal of Analytical Atomic Spectrometry 29, 990–1000.

916 Gillis, K.M., Ludden, J.N., Smith, A.D., 1992. Mobilization of REE during crustal aging in the
917 Troodos Ophiolite, Cyprus. Chemical Geology 98, 71–86.

918 Gillis, K.M., Snow, J.E., Klaus, A., Abe, N., Adrião, Á.B., Akizawa, N., Ceuleneer, G.,
919 Cheadle, M.J., Faak, K., Falloon, T.J., Friedman, S.A., Godard, M., Guerin, G.,
920 Harigane, Y., Horst, A.J., Hoshide, T., Ildefonse, B., Jean, M.M., John, B.E., Koepke, J.,
921 MacHi, S., Maeda, J., Marks, N.E., McCaig, A.M., Meyer, R., Morris, A., Nozaka, T.,
922 Python, M., Saha, A., Wintsch, R.P., 2014. Primitive layered gabbros from fast-
923 spreading lower oceanic crust. Nature 505, 204–207. doi:10.1038/nature12778

924 Godard, M., Dautria, J.M., Perrin, M., 2003. Geochemical variability of the Oman ophiolite
925 lavas: Relationship with spatial distribution and paleomagnetic directions. Geochemistry,
926 Geophysics, Geosystems 4. doi:10.1029/2002GC000452

927 Goodenough, K.M., Thomas, R.J., Styles, M.T., Schofield, D.I., MacLeod, C.J., 2014.
928 Records of ocean growth and destruction in the Oman-UAE ophiolite. Elements 10,
929 109–114. doi:10.2113/gselements.10.2.109

930 Grant, J.A., 1986. The isocon diagram; a simple solution to Gresens equation for
931 metasomatic alteration. Economic geology 81, 1976–1982.

932 Gregory, R.T., Taylor, H.P., 1981. An oxygen isotope profile in a section of Cretaceous
933 oceanic crust, Samail Ophiolite, Oman: Evidence for δ18O buffering of the oceans by
934 deep (> 5 km) seawater- hydrothermal circulation at mid- ocean ridges. Journal of
935 Geophysical Research: Solid Earth 86, 2737–2755.

936 Gresens, R.L., 1967. Composition - Volume Relationships of Metasomatism. Chemical
937 Geology 2, 47–65.

938 Haase, K.M., Freund, S., Beier, C., Koepke, J., Erdmann, M., Hauff, F., 2016. Constraints on
939 the magmatic evolution of the oceanic crust from plagiogranite intrusions in the Oman
940 ophiolite. Contributions to Mineralogy and Petrology 171, 46.

941 Harris, M., Coggon, R.M., Smith-Duque, C.E., Cooper, M.J., Milton, J.A., Teagle, D.A.H.,
942 2015. Channelling of hydrothermal fluids during the accretion and evolution of the upper
943 oceanic crust: Sr isotope evidence from ODP Hole 1256D. Earth and Planetary Science
944 Letters 416, 56–66. doi:10.1016/j.epsl.2015.01.042

945 Hart, S.R., Staudigel, H., 1982. The control of alkalies and uranium in seawater by ocean
946 crust alteration. Earth and Planetary Science Letters 58, 202–212. doi:10.1016/0012-
947 821X(82)90194-7

948 Hasenclever, J., Theissen-Krah, S., Rüpke, L.H., Morgan, J.P., Iyer, K., Petersen, S., Devey,
949 C.W., 2014. Hybrid shallow on-axis and deep off-axis hydrothermal circulation at fast-
950 spreading ridges. Nature 508, 508–512. doi:10.1038/nature13174

951 Heft, K.L., Gillis, K.M., Pollock, M.A., Karson, J.A., Klein, E.M., 2008. Role of upwelling
952 hydrothermal fluids in the development of alteration patterns at fast spreading ridges:
953 Evidence from the sheeted dike complex at Pito Deep. Geochemistry, Geophysics,
954 Geosystems 9. doi:10.1029/2007GC001926

955 Henstock, T.J., Woods, A.W., White, R.S., 1993. The accretion of oceanic crust by episodic
956 sill intrusion. Journal of Geophysical Research: Solid Earth 98, 4143–4161.

957 Hopson, C.A., Coleman, R.G., Gregory, R.T., Pallister, J.S., Bailey, E.H., 1981. Geologic
958 section through the Samail Ophiolite and associated rocks along a Muscat-Ibra
959 Transect, southeastern Oman Mountains. Journal of Geophysical Research 86, 2527.
960 doi:10.1029/JB086iB04p02527

961 Humphris, S.E., Alt, J.C., Teagle, D.A.H., Honnorez, J.J., 1998. Geochemical changes during
962 hydrothermal alteration of basement in the stockwork beneath the active TAG
963 hydrothermal mound, in: PROCEEDINGS OCEAN DRILLING PROGRAM SCIENTIFIC
964 RESULTS. NATIONAL SCIENCE FOUNDATION, pp. 255–276.

965 Jowett, E.C., 1991. Fitting iron and magnesium into the hydrothermal chlorite
966 geothermometer, in: GAC/MAC/SEG Joint Annual Meeting, Toronto, May 27-29, 1991,
967 Program with Abstracts 16.

968 Kelemen, P.B., Koga, K., Shimizu, N., 1997. Geochemistry of gabbro sills in the crust-mantle
969 transition zone of the Oman ophiolite: implications for the origin of the oceanic lower
970 crust. Earth and Planetary Science Letters 146, 475–488. doi:10.1016/S0012-
971 821X(96)00235-X

972 Klinkhammer, G.P., Elderfield, H., Edmond, J.M., Mitra, A., 1994. Geochemical implications
973 of rare earth elements patterns in hydrothermal fluids from mid-ocean ridges.
974 Geochimica et Cosmochimica Acta 58, 5105–5113.

975 Koepke, J., Schoenborn, S., Oelze, M., Wittmann, H., Feig, S.T., Hellebrand, E., Boudier, F.,
976 Schoenberg, R., 2009. Petrogenesis of crustal wehrlites in the Oman ophiolite:
977 Experiments and natural rocks. Geochemistry, Geophysics, Geosystems 10.

978 Kranidiotis, P., MacLean, W.H., 1987. Systematics of chlorite alteration at the Phelps Dodge
979 massive sulfide deposit, Matagami, Quebec. Economic Geology 82, 1898–1911.

980 Lanphere, M.A., Coleman, R.G., Hopson, C.A., 1981. Sr isotopic tracer study of the Samail
981 Ophiolite, Oman. Journal of Geophysical Research: Solid Earth 86, 2709–2720.
982 doi:10.1029/JB086iB04p02709

983 Leake, B.E., Woolley, A.R., Arps, C.E.S., Birch, W.D., Gilbert, M.C., Grice, J.D., Hawthorne,
984 F.C., Kato, A., Kisch, H.J., Krivovichev, V.G., Linthouk, K., 1997. Report. Nomenclature
985 of Amphiboles: Report of the Subcommittee on Amphiboles of the International
986 Mineralogical Association Commission on New Minerals and Mineral Names.

987 Mineralogical Magazine 61, 295–321.

988 MacLean, W.H., 1990. Mass change calculations in altered rock series. Mineralium Deposita
989 25, 44–49.

990 MacLean, W.H., Barrett, T.J., 1993. Lithogeochemical techniques using immobile elements.
991 Journal of geochemical exploration 48, 109–133.

992 MacLean, W.H., Kranidiotis, P., 1987. Immobile elements as monitors of mass transfer in
993 hydrothermal alteration; Phelps Dodge massive sulfide deposit, Matagami, Quebec.
994 Economic Geology 82, 951–962.

995 Maclennan, J., Hulme, T., Singh, S.C., 2004. Thermal models of oceanic crustal accretion:
996 Linking geophysical, geological and petrological observations. Geochemistry,
997 Geophysics, Geosystems 5. doi:10.1029/2003GC000605

998 MacLeod, C.J., Lissenberg, C.J., Bibby, L.E., 2013. “Moist MORB” axial magmatism in the
999 Oman ophiolite: The evidence against a mid-ocean ridge origin. Geology 41, 459–462.

1000 MacLeod, C.J., Yaouancq, G., 2000. A fossil melt lens in the Oman ophiolite: Implications for
1001 magma chamber processes at fast spreading ridges. Earth and Planetary Science
1002 Letters 176, 357–373.

1003 Manning, C.E., MacLeod, C.J., Weston, P.E., 2000. Lower-crustal cracking front at fast-
1004 spreading ridges: Evidence from the East Pacific Rise and the Oman ophiolite. Special
1005 Papers-Geological Society of America 261–272.

1006 Manning, C.E., Weston, P.E., Mahon, K.I., 1996. Rapid high-temperature metamorphism of
1007 East Pacific Rise gabbros from Hess Deep. Earth and Planetary Science Letters 144,
1008 123–132.

1009 McArthur, J.M., Howarth, R.J., Bailey, T.R., 2001. Strontium isotope stratigraphy: LOWESS
1010 version 3: best fit to the marine Sr-isotope curve for 0-509 Ma and accompanying look-
1011 up table for deriving numerical age. The Journal of Geology 109, 155–170.

McCulloch, M.T., Gregory, R.T., Wasserburg, G.J., Taylor, H.P., 1981. Sm-Nd, Rb-Sr, and 18O/16O isotopic systematics in an oceanic crustal section: Evidence from the Samail Ophiolite. Journal of Geophysical Research: Solid Earth 86, 2721–2735.

McCulloch, M.T., Gregory, R.T., Wasserburg, G.J., Taylor, H.P.J., 1980. A Neodymium, Strontium, and Oxygen Isotopic Study of the cretaceous Samail ophiolite and implications for the petrogenesis and seawater-hydrothermal alteration of oceanic crust. Earth and Planetary 46, 201–211.

McDowell, S.D., Elders, W.A., 1980. Authigenic layer silicate minerals in borehole Elmore 1, Salton Sea geothermal field, California, USA. Contributions to mineralogy and petrology 74, 293–310.

Morgan, J.P., Chen, Y.J., 1993. The genesis of oceanic crust: Magma injection, hydrothermal circulation, and crustal flow. Journal of Geophysical Research: Solid Earth 98, 6283–6297.

Morton, J.L., Sleep, N.H., 1985. A mid- ocean ridge thermal model: Constraints on the volume of axial hydrothermal heat flux. Journal of Geophysical Research: Solid Earth 90, 11345–11353.

Mueller, S., Koepke, J., Garbe-Schoenberg, C.D., Müller, T., Mock, D., Strauss, H., Schuth, S., Ildefonse, B., 2017. A Reference Section through the Lower Fast-spreading Oceanic Crust in the Wadi Gideah (Sumail ophiolite, Sultanate Oman): Drill Sites GT1A and GT2A within the ICDP Oman Drilling Project, in: AGU Fall Meeting Abstracts.

Müller, T., 2016. A petrological and geochemical cross section of lower crust at the Wadi Gideah (Samail ophiolite): Implications for the crustal accretion at fast-spreading mid-ocean ridges (PhD thesis). Gottfried Wilhelm Leibniz Universität Hannover, Géosciences Montpellier Université Montpellier.

Müller, T., Koepke, J., Garbe-Schönberg, C.-D., Dietrich, M., Bauer, U., Wolff, P.E., 2017. Anatomy of a frozen axial melt lens from a fast-spreading paleo-ridge (Wadi Gideah,

1038 Oman ophiolite). Lithos 272, 31–45.

1039 Nehlig, P., Juteau, T., 1988. Deep crustal seawater penetration and circulation at ocean
1040 ridges: Evidence from the Oman ophiolite. Marine Geology 84, 209–228.

1041 Nehlig, P., Juteau, T., Bendel, V., Cotten, J., 1994. The root of oceanic hydrothermal
1042 systems: Constraints from the Semail ophiolite (Oman). Journal of Geophysical
1043 Research 99, 4703–4713. doi:10.1029/93JB02663

1044 Nicolas, A., Boudier, F., Ildefonse, B., Ball, E., 2000. Accretion of Oman and United Arab
1045 Emirates ophiolite--Discussion of a new structural map. Marine Geophysical
1046 Researches 21, 147–180.

1047 Nicolas, A., Mainprice, D., Boudier, F., 2003. High-temperature seawater circulation
1048 throughout crust of oceanic ridges: A model derived from the Oman ophiolites. Journal
1049 of Geophysical Research 108, 2371.

1050 Oeser, M., Strauss, H., Wolff, P.E., Koepke, J., Peters, M., Garbe-Schönberg, D., Dietrich,
1051 M., 2012. A profile of multiple sulfur isotopes through the Oman ophiolite. Chemical
1052 Geology 312, 27–46.

1053 Pallister, J.S., 1981. Structure of the sheeted dike complex of the Samail ophiolite near Ibra,
1054 Oman. Journal of Geophysical Research: Solid Earth 86, 2661–2672.

1055 Pallister, J.S., Hopson, C.A., 1981. Samail ophiolite plutonic suite: field relations, phase
1056 variation, cryptic variation and layering, and a model of a spreading ridge magma
1057 chamber. Journal of Geophysical Research: Solid Earth 86, 2593–2644.

1058 Pallister, J.S., Knight, R.J., 1981. Rare- earth element geochemistry of the Samail Ophiolite
1059 near Ibra, Oman. Journal of Geophysical Research: Solid Earth 86, 2673–2697.

1060 Palmer, M.R., Edmond, J.M., 1989. The strontium isotope budget of the modern ocean.
1061 Earth and Planetary Science Letters 92, 11–26.

1062 Palmer, M.R., Edmond, J.M., 1989. Cesium and rubidium in submarine hydrothermal fluids:

1063 evidence for recycling of alkali elements. Earth and Planetary Science Letters 95, 8–14.
1064 doi:10.1016/0012-821X(89)90163-5

1065 Peters, T., El Amin, O., Blechschmid, I., Al-Busaidi, S., 2008. Geological Map Oman
1066 1:50000, Sheet NF 40-8A1. Sultanate of Oman: Ministry of Commerce and Industry.

1067 Peucker-Ehrenbrink, B., Hanghoj, K., Atwood, T., Kelemen, P.B., 2012. Rhenium-osmium
1068 isotope systematics and platinum group element concentrations in oceanic crust.
1069 Geology 40, 199–202. doi:10.1130/G32431.1

1070 Pin, C., Briot, D., Bassin, C., Poitrasson, F., 1994. Concomitant separation of strontium and
1071 samarium-neodymium for isotopic analysis in silicate samples, based on specific
1072 extraction chromatography. Analytica Chimica Acta 298, 209–217.

1073 Quick, J.E., Denlinger, R.P., 1993. Ductile deformation and the origin of layered gabbro in
1074 ophiolites. Journal of Geophysical Research: Solid Earth 98, 14015–14027.

1075 Richardson, C.J., Cann, J.R., Richards, H.G., Cowan, J.G., 1987. Metal-depleted root zones
1076 of the Troodos ore-forming hydrothermal systems, Cyprus. Earth and Planetary Science
1077 Letters 84, 243–253.

1078 Rioux, M., Bowring, S., Kelemen, P., Gordon, S., Miller, R., Dudás, F., 2013. Tectonic
1079 development of the Samail ophiolite: High-precision U-Pb zircon geochronology and
1080 Sm-Nd isotopic constraints on crustal growth and emplacement. Journal of Geophysical
1081 Research: Solid Earth 118, 2085–2101.

1082 Schiffman, P., Smith, B.M., Varga, R.J., Moores, E.M., 1987. Geometry, conditions and
1083 timing of off-axis hydrothermal metamorphism and ore-deposition in the Solea graben.
1084 Nature 325, 423.

1085 Searle, M., Cox, J., 1999. Tectonic setting, origin, and obduction of the Oman ophiolite.
1086 Geological Society of America Bulletin 111, 104–122.

1087 Seewald, J.S., Seyfried, W.E., 1990. The effect of temperature on metal mobility in

1088 subseafloor hydrothermal systems: constraints from basalt alteration experiments. Earth
1089 and Planetary Science Letters 101, 388–403. doi:10.1016/0012-821X(90)90168-W

1090 Sleep, N.H., 1991. Hydrothermal circulation, anhydrite precipitation, and thermal structure at
1091 ridge axes. Journal of Geophysical Research: Solid Earth 96, 2375–2387.

1092 Staudigel, H., 2014. Chemical fluxes from hydrothermal alteration of the oceanic crust, in:
1093 Rudnick, R.L. (Ed.), Treatise on Geochemistry, 2nd Edition The Crust Vol. 4, Elsevier,
1094 Oxford. Elsevier, pp. 583–606.

1095 Staudigel, H., Plank, T., White, B., Schmincke, H., 1996. Geochemical fluxes during seafloor
1096 alteration of the basaltic upper oceanic crust: DSDP Sites 417 and 418. Subduction: top
1097 to bottom 96, 19–38.

1098 Sun, C., Lissenberg, C.J., 2018. Formation of fast-spreading lower oceanic crust as revealed
1099 by a new Mg–REE coupled geospeedometer. Earth and Planetary Science Letters 487,
1100 165–178.

1101 Teagle, D.A.H., Alt, J.C., 2004. Hydrothermal alteration of basalts beneath the Bent Hill
1102 massive sulfide deposit, Middle Valley, Juan de Fuca Ridge. Economic Geology 99,
1103 561–584.

1104 Teagle, D.A.H., Alt, J.C., Bach, W., Halliday, A.N., Erzinger, J., 1996. Alteration of upper
1105 ocean crust in a ridge-flank hydrothermal upflow zone: mineral, chemical, and isotopic
1106 constraints from Hole 896A, in: Proceedings-Ocean Drilling Program, Scientific Results.
1107 National Science Foundation, pp. 119–150.

1108 Teagle, D.A.H., Bickle, M.J., Alt, J.C., 2003. Recharge flux to ocean-ridge black smoker
1109 systems: a geochemical estimate from ODP Hole 504B. Earth and Planetary Science
1110 Letters 210, 81–89.

1111 Theissen-Krah, S., Rüpke, L.H., Hasenclever, J., 2016. Modes of crustal accretion and their
1112 implications for hydrothermal circulation. Geophysical Research Letters 43, 1124–1131.

1113 doi:10.1002/2015GL067335

1114 Toy, V.G., Sutherland, R., Townend, J., Allen, M.J., Becroft, L., Boles, A., Boulton, C.,
1115 Carpenter, B., Cooper, A., Cox, S.C., Daube, C., Faulkner, D.R., Halfpenny, A., Kato,
1116 N., Keys, S., Kirilova, M., Kometani, Y., Little, T., Mariani, E., Melosh, B., Menzies, C.D.,
1117 Morales, L., Morgan, C., Mori, H., Niemeijer, A., Norris, R., Prior, D., Sauer, K.,
1118 Schleicher, A.M., Shigematsue, N., Teagle, D.A.H., Tobin, H., Valdez, R., Williams, J.,
1119 Yeo, S., Baratin, L.-M., Barth, N., Benson, A., Boese, C., Célérier, B., Chamberlain,
1120 C.J., Conze, R., Coussens, J., Craw, L., Doan, M.-L., Eccles, J., Grieve, J., Grochowski,
1121 J., Gulley, A., Howarth, J., Jacobs, K., Janku-Capova, L., Jeppson, T., Langridge, R.,
1122 Mallyon, D., Marx, R., Massiot, C., Mathewson, L., Moore, J., Nishikawa, O., Pooley, B.,
1123 Pyne, A., Savage, M.K., Schmitt, D., Taylor-Offord, S., Upton, P., Weaver, K.C.,
1124 Wiersberg, T., Zimmer, M., DFDP-2-Science Team, 2017. Bedrock geology of DFDP-
1125 2B, central Alpine Fault, New Zealand. New Zealand Journal of Geology and
1126 Geophysics 60, 497–518.

1127 VanTongeren, J.A., Kelemen, P.B., Hanghøj, K., 2008. Cooling rates in the lower crust of the
1128 Oman ophiolite: Ca in olivine, revisited. Earth and Planetary Science Letters 267, 69–
1129 82. doi:10.1016/j.epsl.2007.11.034

1130 Velde, B., Hillier S, 1991. Octahedral occupancy and the chemical composition of diagenetic
1131 (low-temperature) chlorites. Clay Minerals 26, 149–168.

1132 Vogel, W., Kuipers, G., 1987. A pre-calibrated program for geological applications. Phillips
1133 New Developments in X-Ray Spectrometry 11, 2–8.

1134 Von Damm, K.L., 1995. Controls on the chemistry and temporal variability of seafloor
1135 hydrothermal fluids. Seafloor hydrothermal systems: physical, chemical, biological, and
1136 geological interactions 222–247.

1137 Von Damm, K.L., Bischoff, J.L., Rosenbauer, R.J., 1991. Quartz solubility in hydrothermal
1138 seawater; an experimental study and equation describing quartz solubility for up to 0.5

M NaCl solutions. American Journal of Science 291, 977–1007.

Warren, C.J., Parrish, R.R., Waters, D.J., Searle, M.P., 2005. Dating the geologic history of Oman's Semail ophiolite: Insights from U-Pb geochronology. Contributions to Mineralogy and Petrology 150, 403–422. doi:10.1007/s00410-005-0028-5

Warren, C.J., Searle, M.P., Parrish, R.R., Waters, D.J., 2007. Reply to Comment by F. Boudier and A. Nicolas on "dating the geologic history of Oman's Semail Ophiolite: Insights from U-Pb geochronology" by C.J. Warren, R.R. Parrish, M.P. Searle and D.J. Waters. Contributions to Mineralogy and Petrology 154, 115–118. doi:10.1007/s00410-007-0182-z

Weyhenmeyer, C.E., 2000. Origin and evolution of groundwater in the alluvial aquifer of the Eastern Batinah Coastal Plain, Sultanate of Oman. PhD., University of Bern, Switzerland.

White, W.M., Hofmann, a. W., Puchelt, H., 1987. Isotope geochemistry of Pacific Mid-Ocean Ridge Basalt. Journal of Geophysical Research 92, 4881. doi:10.1029/JB092iB06p04881

Xie, X., Byerly, G.R., Ferrell Jr, R.E., 1997. IIb trioctahedral chlorite from the Barberton greenstone belt: crystal structure and rock composition constraints with implications to geothermometry. Contributions to Mineralogy and Petrology 126, 275–291.

Xie, Z., Walther, J. V, 1993. Wollastonite+ quartz solubility in supercritical NaCl aqueous solutions. American journal of Science 293, 235.

List of Tables – with captions

Table 1: Mineral paragenesis, whole rock major- and trace element data and Sr-isotope data of all samples.

Table 2: Major and trace element summary of mass changes calculated in wt. %/ µg/g and percent relative to fresh layered gabbro.

Table 3: Comparison of estimated hydrothermal net fluxes in (+) and out (-) of the lower oceanic crust due to faulting in comparison with extrapolated global hydrothermal from Macquarie island ophiolite (Coggon et al., 2016) and a composite section (Staudigel, 2014). Significant fluxes (magnitude at least 10% of background hydrothermal flux) are highlighted in light green.

1171 *Table 1*

Typ			fresh background gabbro[1]	hanging wall	hanging wall	foot wall	clast	clast	fault rock	fault rock	fault rock	fault rock	fault rock	fault rock	fault rock	fault rock
Sample ID			md ± MAD (n=8)[2]	AH9	OM15-3A*	OM15-3F *	AH6	AH7	AD5	AD6	AD7	DT-10	OM15-3C*	OM15_3E*	AH8	
Mineral assemblage	Primary minerals		plagiocalse, clinopyroxene, olivine ± oxides	clinopyroxene and plagioclase partially preserved	clinopyroxene and plagioclase partially preserved	clinopyroxene and plagioclase partially well preserved	clinopyroxene and plagioclase partially preserved	clinopyroxene and plagioclase only rarely preserved	no primary minerals preserved	no primary minerals preserved	no primary minerals preserved	no primary minerals preserved	no primary minerals preserved	no primary minerals preserved	some clinopyroxene relics preserved	
	Secondary minerals		± chlorite, ± Mg-hornblende, ± tremolite	albite, Mg-hornblende, actinolite, chlorite, prehnite, laumontite	prehnite, chlorite, laumontite, tremolite, Mg-hornblende, pumpellyite	chlorite, tremolite, Mg-hornblende, oxides	albite, Mg-hornblende, actinolite, chlorite, laumontite carbonate, ± epidote, ± titanite	chlorite, albite, Mg-hornblende, actinolite, epidote	chlorite, epidote, titanite	chlorite, epidote, titanite	chlorite, epidote, titanite, chalcopyrite	chlorite	chlorite	chlorite, epidote	chlorite, epidote, titanite	
	Weathering minerals		-	minor amount of Fe-hydroxides, calcite	calcite, Fe-hydroxides	-	-	calcite	Fe-hydroxides, calcite	Fe-hydroxides,malachite, calcite	Fe-hydroxides,malachite, calcite	Fe-hydroxides,malachite, calcite	Fe-hydroxides,malachite, native Cu, calcite	calcite, malachite	Fe-hydroxides,malachite, calcite	
	Vein	hornblende					x									
		tremolite				x										
		chlorite				x										
		prehnite		x	x											
		zeolite		x	x		x	x	x	x	x	x	x	x	x	
		calcite		x	x		x	x	x	x	x	x	x	x	x	
SiO_2	wt. %	XRF	46.72 ± 0.6	45.2	43.4	46.5	46.8	49.6	26.5	26	30.1	23.2	27.2	22.7	26.9	
Al_2O_3	wt. %	XRF	17.99 ± 0.7	17.8	16.0	13.6	19.1	15.8	19.6	19.4	20.9	14.5	19.2	14.7	18.9	
Fe_2O_3	wt. %	XRF	5.28 ± 0.4	5.7	3.2	5.8	3.3	6.6	28	30	22.4	32.1	27.6	16.7	22.7	
MnO	wt. %	XRF	0.09 ± 0.01	0.1	0.1	0.1	0.1	0.1	0.3	0.3	0.2	0.2	0.3	0.2	0.2	
MgO	wt. %	XRF	10.58 ± 1.2	11.2	8.1	11.8	8.5	10.8	13.8	13.3	11.8	8.4	13	12.7	18.1	
CaO	wt. %	XRF	16.44 ± 0.4	12.6	16.1	15.3	15.5	6.5	2.7	0.9	4.7	0.4	1.6	13.7	0.2	
Na_2O	wt. %	XRF	0.99 ± 0.1	1.5	1	0.8	1.4	1.6	0.1	0.1	0.1	0.6	< 0.2	0.5	0.1	
K_2O	wt. %	XRF	<0.02	< 0.01	0.0	0.0	< 0.01	< 0.01	< 0.01	< 0.01	< 0.01	0.0	< 0.02	< 0.02	< 0.01	
TiO_2	wt. %	XRF	0.22 ± 0.02	0.2	0.2	0.2	0.2	0.4	0.3	0.5	0.3	0.1	0.3	0.6	0.3	
P_2O_5	wt. %	XRF	<0.08	0.01	< 0.08	< 0.08	0.01	0.02	0.02	0.03	0.01	0.1	0.01	0.1	0.01	
SO_3	wt. %	XRF	-	< 0.01	0.00	0.01	< 0.01	0.02	0.01	< 0.01	< 0.01	0.01	0.01	0.02	< 0.01	
LOI[3]	wt. %	XRF	1.95 ± 0.2	5.6	11.0	5.6	5	14.6	8.6	8.8	8.9	11.2	10.9	17.2	13.6	
Total	wt. %	XRF	100.00	99.8	99.1	99.7	99.8	99.6	99.8	99.2	99.5	90.8	100	99.1	99.8	
Mg#			88-90	88.6	91	89	91.1	86.8	66.2	63.8	67.6	50.8	65.1	75.1	75.9	
Li	µg/g	ICP-MS / LA-ICP MS	0.82 ± 0.2	0.7	0.4	0.3	0.2	1.1	0.8	0.6	1	0.8	2.2	1.4	0.9	
Sc	µg/g	ICP-MS / LA-ICP MS	41.77 ± 6.4	33.3	33.5	46.7	39.7	51.7	53.7	51.1	44.6	27.7	50.1	51.1	44.8	
V	µg/g	ICP-MS / LA-ICP MS	119.74 ± 20.9	84.3	117.6	149.2	107.3	113.5	167.6	219.7	124.5	1547	222.3	238.5	131.2	
Cr	µg/g	XRF / LA ICP-MS	685.34 ± 109.3	548.2	366.6	651.2	437.7	798.1	581.4	642.5	531.1	409	743.8	806.4	1140.7	
Co	µg/g	XRF / LA ICP-MS	40.32 ± 4.6	45.6	21.3	41.1	9.9	54.5	131.8	344	112.3	161	175.3	105.1	121.5	
Ni	µg/g	XRF / LA ICP-MS	172.15 ± 30.1	194.4	118.6	172.7	113.2	146.2	168.9	182.2	147.4	200.3	241	247.8	240	
Cu	µg/g	ICP-MS / LA-ICP MS	119.71 ± 30.4	92.8	6.4	196.4	44	1339	76.7	4557	3406.0	75790	6514.2	34.6	8.8	
Zn	µg/g	ICP-MS / LA-ICP MS	21.68 ± 1	23.3	6.8	18.2	10.5	88.1	147.3	161.5	168.6	1141	366.1	170.8	119	
Rb	µg/g	ICP-MS / LA-ICP MS	0.08 ± 0.01	0.1	0.1	0.1	0.1	0.1	0.0	0.01	0.02	0.02	0.1	0.1	0.01	

Sr	µg/g	ICP-MS / LA-ICP MS	139.16 ± 2.8	179.5	221.1	89.7	292.9	105.7	81.7	21.4	53.7	15.7	50.4	54.6	22.8
Y	µg/g	XRF / LA ICP-MS	4.32 ± 0.5	6.6	4.2	5.8	7.8	10.1	7.5	13.2	5.9	3.0	6.4	12	8.1
Zr	µg/g	XRF / LA ICP-MS	3.21 ± 0.3	7.6	2.9	3.7	8.3	13.6	5.1	16.5	6.0	4.8	4.8	-	11.1
Cs	µg/g	ICP-MS / LA-ICP MS	<0.01	0.002	0.004	0.003	0.001	0.001	0.001	<0.0003	0.002	0.001	0.007	0.003	<0.0003
Ba	µg/g	ICP-MS / LA-ICP MS	2.21 ± 0.2	5.5	3.1	7.4	9.3	3.6	<0.45	<0.45	3.7	0.6	14	9	<0.45
La	µg/g	ICP-MS / LA-ICP MS	0.21 ± 0.02	0.1	-	0.2	0.1	0.2	0.9	0.2	0.3	0.1	0.2	0.6	0.1
Ce	µg/g	ICP-MS / LA-ICP MS	0.63 ± 0.1	0.5	-	-	0.5	0.8	2.8	1.0	0.8	0.5	0.7	2.7	0.5
Pr	µg/g	ICP-MS / LA-ICP MS	0.14 ± 0.02	0.1	0.1	0.2	0.1	0.2	0.5	0.2	0.2	0.1	0.1	0.5	0.1
Nd	µg/g	ICP-MS / LA-ICP MS	0.93 ± 0.1	0.7	0.8	1	0.8	1.3	2.9	1.4	1.1	0.6	0.9	3.1	1.0
Sm	µg/g	ICP-MS / LA-ICP MS	0.44 ± 0.1	0.3	0.4	0.5	0.4	0.6	0.9	0.8	0.5	0.3	0.5	1.3	0.5
Eu	µg/g	ICP-MS / LA-ICP MS	0.29 ± 0.01	0.2	0.2	0.3	0.2	0.4	0.4	0.2	0.2	0.1	0.2	0.5	0.2
Gd	µg/g	ICP-MS / LA-ICP MS	0.68 ± 0.1	0.5	0.6	0.8	0.7	1	1.2	1.4	0.8	0.5	0.8	1.7	0.8
Tb	µg/g	ICP-MS / LA-ICP MS	0.12 ± 0.02	0.1	-	-	0.1	0.2	0.2	0.3	0.2	0.1	0.2	0.3	0.2
Dy	µg/g	ICP-MS / LA-ICP MS	0.83 ± 0.1	0.7	0.7	1.1	0.8	1.3	1.3	1.8	1.0	0.7	1.2	2.1	1
Ho	µg/g	ICP-MS / LA-ICP MS	0.18 ± 0.02	0.1	0.2	0.2	0.2	0.3	0.3	0.4	0.2	0.2	0.3	0.4	0.2
Er	µg/g	ICP-MS / LA-ICP MS	0.47 ± 0.1	0.4	0.4	0.6	0.5	0.8	0.8	1.1	0.6	0.5	0.7	1.3	0.6
Tm	µg/g	ICP-MS / LA-ICP MS	0.07 ± 0.01	0.1	0.1	0.1	0.1	0.1	0.1	0.2	0.1	0.1	0.1	0.2	0.1
Yb	µg/g	ICP-MS / LA-ICP MS	0.41 ± 0.1	0.3	0.4	0.5	0.4	0.7	0.7	0.9	0.5	0.5	0.6	1.2	0.5
Lu	µg/g	ICP-MS / LA-ICP MS	0.06 ± 0.01	0.1	0.1	0.1	0.1	0.1	0.1	0.1	0.1	0.1	0.1	0.2	0.1
Hf	µg/g	ICP-MS / LA-ICP MS	0.15 ± 0.02	0.3	0.1	0.2	0.3	0.3	0.2	0.4	0.2	0.2	0.2	-	0.4
Pb	µg/g	ICP-MS / LA-ICP MS	10.83 ± 10.6	<0.08	0.03	0.1	<0.08	<0.08	<0.08	0.5	0.1	3.3	0.7	0.2	<0.08
Th	µg/g	ICP-MS / LA-ICP MS	<0.005	0.01	0.003	0.004	0.01	0.01	0.01	0.02	0.01	0.02	0.01	0.08	0.01
U	µg/g	ICP-MS / LA-ICP MS	<0.005	0.02	0.01	0.01	0.01	0.06	0.02	0.6	0.05	10.2	0.2	0.04	0.01
$^{87}Sr/^{86}Sr$ measured				0.703903	0.704756	0.703274	0.704510	0.704969	0.704553	-	0.704742	0.705480	0.704745	0.704802	-
$^{87}Sr/^{86}Sr$ 95 Ma				0.703900	0.704754	0.703269	0.704508	0.704965	0.704553	-	0.704741	0.705444	0.704741	0.704792	-
± 2 SE (error)				14	13	14	16	16	16	-	16	14	12	11	-

Picked minerals	**foot wall epidote (vein)**	**hanging wall laumontite (vein)**	**hanging wall calcite (vein)**	**fault rock calcite (vein)**
$^{87}Sr/^{86}Sr$ measured	0.704280	0.707378	0.708242	0.707778
$^{87}Sr/^{86}Sr$ 95 Ma	0.704279	0.707366	0.708233	0.707767
± 2 SE	14	17	14	14

[1)] major elements measured with ICP-OES , trace elements measured with liq.-ICP-MS and LA-ICP-MS, for details see table A1 for detail

[2)] median ± median absolute deviation, see Table A1 for detail

[3)] LOI determined by loss-on-ignition experiment at 1000 °C

* trace elements measured with LA-ICP-MS on pressed powder tablets

1172

1173 **Table 2**

	Layered gabbro	hanging wall				foot wall				clast					
	median (n=8)	AH9		OM15-3A		OM15-3F		*Med (n=3)*	*MAD (n=3)*	AH6		AH7		Med (n=2)	*MAD (n=2)*
		wt. % µg/g	%	wt. % µg/g	%	wt. % µg/g	%	%		wt. % µg/g	%	wt. % µg/g	%	%	%
SiO_2	**46.62**	9.1	19.4	0.7	1.5	-10.5	-22.5	**1.5**	**14**	-1.8	-3.8	-16	-34.3	**-19**	**15.3**
Al_2O_3	**17.89**	4	22.2	-0.5	-2.7	-7.4	-41.4	**-2.7**	**21.2**	0.3	1.9	-8.2	-45.6	**-21.8**	**23.8**
Fe_2O_3	**5.05**	1.7	32.8	-1.8	-34.9	-0.8	-15	**-15**	**22.6**	-2.1	-40.4	-1.2	-23.2	**-31.8**	**8.6**
MnO	**0.09**	0.03	32.4	-0.03	-29	-0.006	-7.2	**-7.2**	**20.5**	-0.04	-46.1	-0.05	-49.8	**-48**	**1.9**
MgO	**10.68**	3.2	30.5	-1.8	-16.6	-1.4	-13.2	**-13.2**	**15.7**	-2.4	-22.8	-3.9	-36.6	**-29.7**	**6.9**
CaO	**16.38**	-0.9	-5.4	1.1	6.6	-4.6	-27.7	**-5.4**	**11.4**	-1.5	-9.2	-12.4	-75.5	**-42.4**	**33.2**
Na_2O	**0.99**	0.8	84.4	0.1	14.5	-0.4	-35.7	**14.5**	**40**	0.4	37	0.09	0.9	**19**	**18**
TiO_2	**0.22**	-0.03	-14.4	-0.03	-12.1	-0.05	-20.9	**-14.4**	**2.9**	-0.03	-12.2	0.02	8.7	**-1.8**	**10.5**
LOI	**2.07**	5	255.3	10	515.5	2.4	122.8	**255.3**	**130.9**	2.9	147.1	7.1	363.3	**255.2**	**108.1**
Li	**0.81**	0.1	8.9	-0.4	-45.2	-0.6	-68.6	**-45.2**	**25.8**	-0.6	-71.7	-0.1	-14.4	**-43**	**28.6**
Sc	**42.51**	-0.7	-1.7	-5.2	-12.5	-5.4	-13	**-12.5**	**3.8**	-3.6	-8.6	-9.8	-23.4	**-16**	**7.4**
V	**120.73**	-15.7	-13.1	8.6	7.2	-3.6	-3	**-3**	**6.8**	-16.6	-13.8	-49.5	-41.3	**-27.6**	**13.7**
Cr	**692.33**	-8.7	-1.3	-285.2	-41.6	-178.6	-26.1	**-26.1**	**13.5**	-264.5	-38.6	-191.2	-27.9	**-33.3**	**5.3**
Co	**37.52**	16	39.6	-17.1	-42.4	-8.4	-20.7	**-20.7**	**27.4**	-30.8	-76.4	-6.6	-16.3	**-46.4**	**30**
Ni	**176.69**	67.8	39.4	-42.7	-24.8	-37.8	-21.9	**-21.9**	**21.4**	-63.4	-36.8	-81.7	-47.4	**-42.1**	**5.3**
Cu	**126.58**	-5.2	-4.3	-112.7	-94.2	-58.2	-48.6	**-48.6**	**29.9**	-77.4	-64.6	709.3	592.5	**263.9**	**328.6**
Zn	**20.76**	4.1	18.7	-14.3	-65.8	-7.5	-34.7	**-34.7**	**28.2**	-12.6	-58.1	25.4	117	**29.5**	**87.6**
Rb	**0.07**	-0.006	-7.3	0.1	100.3	-0.01	-9.4	**-7.3**	**36.6**	-0.03	-35	0.0	-49.6	**-42.3**	**7.3**
Sr	**134.01**	82.4	59.2	102.2	73.4	-69.4	-49.9	**59.2**	**41.1**	142.5	102.4	-73.7	-53	**24.7**	**77.7**
Y	**4.28**	3.8	88.5	0.3	6.5	0.2	3.6	**6.5**	**28.3**	3.2	73.5	1.9	44.6	**59.1**	**14.4**
Zr	**3.41**	6.2	192	-0.03	-1	-0.4	-11.2	**-1**	**67.7**	4.8	148.4	5.2	162	**155.2**	**6.8**
Cs[1)]	**0.005**	-0.002	-49.7	<-0.0001	-19.5	-0.003	-59.9	**-49.7**	**13.5**	-0.003	-80.4	-0.004	-87.4	**-83.9**	**3.5**
Ba	**2.34**	4.6	209.3	1.2	52.3	3.6	161.4	**161.4**	**52.3**	6.7	302.7	0.02	1	**151.8**	**150.9**

La	**0.22**	-0.04	-20.8	-	-	-0.03	-12.2	**-16.5**	**8.4**	-0.1	-51.8	-0.1	-38.8	**-45.3**	**6.5**	
Ce	**0.66**	-0.003	-0.5	-	-	-	-	**-0.5**	**0.3**	-0.2	-31.1	-0.1	-21.7	**-26.4**	**4.7**	
Pr	**0.13**	-0.01	-4.1	-0.01	-10.7	-0.02	-11.1	**-10.7**	**2.3**	-0.03	-21.9	-0.02	-12.8	**-17.3**	**4.5**	
Nd	**0.9**	-0.04	-4.2	-0.1	-8.9	-0.1	-16	**-8.9**	**3.9**	-0.2	-19.4	-0.1	-12.2	**-15.8**	**3.6**	
Sm	**0.43**	-0.04	-9	-0.03	-6.2	0.0	-7.7	**-7.7**	**0.9**	-0.1	-12.5	-0.1	-13.4	**-13**	**0.4**	
Eu	**0.27**	-0.02	-7.4	-0.1	-20.5	-0.1	-23.7	**-20.5**	**5.4**	-0.1	-32.9	-0.1	-24.5	**-28.7**	**4.2**	
Gd	**0.66**	-0.03	-4.6	-0.1	-8.5	-0.05	-6.8	**-6.8**	**1.3**	-0.1	-7.6	-0.1	-9.7	**-8.6**	**1**	
Tb	**0.12**	-0.01	-4.2	-	-	-	-	**-4.2**	**2.8**	-0.01	-4.6	-0.01	-5.4	**-5**	**0.4**	
Dy	**0.81**	-0.02	-2.9	-0.03	-3.3	-0.01	-1	**-2.9**	**0.8**	-0.02	-2.2	-0.04	-5.2	**-3.7**	**1.5**	
Ho	**0.17**	-0.002	-1.2	-0.01	-3.4	-0.001	-0.3	**-1.2**	**1**	0.00	-1.7	-0.01	-4	**-2.9**	**1.2**	
Er	**0.47**	-0.003	-0.7	-0.003	-0.6	0.002	0.4	**-0.6**	**0.4**	0.01	1.2	0.003	0.5	**0.9**	**0.3**	
Tm	**0.07**	0.001	0.9	0.001	2.1	-0.001	-0.9	**0.9**	**1**	0.0003	0.4	0.0002	0.3	**0.3**	**0.1**	
Yb	**0.42**	0.01	2.3	0.02	4.3	0.004	0.9	**2.3**	**1.1**	0.02	4.3	0.02	4.6	**4.4**	**0.1**	
Lu	**0.06**	0.001	1.5	0.001	1	0.001	0.9	**1**	**0.2**	-0.001	-1.9	0.002	3.9	**1**	**2.9**	
Hf	**0.15**	0.2	135.7	-0.01	-7.3	-0.02	-10.7	**-7.3**	**48.8**	0.1	83	0.02	11.8	**47.4**	**35.6**	
Pb	**14.82**	-	-	-10.8	-99.7	-10.7	-99.1	**-99.4**	**50**	-	-	-	-		**-**	
U	**0.01**	0.02	354.8	0.007	124.6	-0.001	-10.3	**124.6**	**121.7**	0.01	119.3	0.03	551.7	**335.5**	**216.2**	
mass change term		0.8		0.9		1.3		**1.0**		1.0		1.6		**1.3**		
total mass change (%)								**-1.1**						**-33.7**		

chlorite fault rock

	AD5		**AD6**		**AD7**		**DT-10**		**OM15-3C**		**OM15_3E**		**AH8**		**Med (n=7)**	***MAD (n=7)***
	wt. % µg/g	**%**	**wt. % µg/g**	**%**	**wt. % µg/g**	**%**	**wt. % µg/g**	**%**	**wt. % µg/g**	**%**	**wt. % µg/g**	**%**	**wt. % µg/g**	**%**		**%**
SiO_2	-30.4	-65.1	-35.1	-75.2	-23.1	-49.5	-23.3	-49.8	-28.7	-61.5	-38.2	-81.8	-25	-53.6	**-61.5**	**9.9**
Al_2O_3	-5.9	-32.8	-9.3	-51.9	-1.6	-8.8	-3.3	-18.6	-5.3	-29.7	-12.5	-69.5	-2.7	-15.1	**-29.7**	**16**
Fe_2O_3	11.9	225.8	8.1	153.4	12.3	232.8	27.2	514.7	13	245.5	1	18.2	13.1	247.3	**232.8**	**87.2**
MnO	0.1	79.5	0.02	22.3	0.1	91	0.1	97	0.1	84.8	-0.003	-2.7	0.1	107.9	**84.8**	**28.1**
MgO	-2.1	-19.6	-4.6	-43.8	-1.3	-12.5	-2.1	-19.9	-2	-18.7	-5.8	-55	4	38.1	**-19.6**	**17.9**
CaO	-14.8	-89.9	-16.1	-97.6	-12.8	-77.5	-16	-97.4	-15.4	-93.6	-11.3	-68.8	-16.3	-99.2	**-93.6**	**8.3**

Na_2O	-0.9	-94.7	-0.9	-95.3	-0.9	-92.9	-0.4	-37.8			-0.8	-81.5	-0.9	-90.9	**-90.9**	**23.4**
TiO_2	-0.1	-25.9	-0.03	-13.7	-0.03	-14.1	-0.1	-43.6	-0.1	-24.7	0.003	1.4	0.0	5	**-14.1**	**12.4**
LOI	3.3	170.9	2	102.1	5.1	259.6	9.3	480.6	5.2	269.7	4.5	229.9	9	464.2	**259.6**	**101.7**
Li	-0.3	-37.3	-0.6	-67.0	-0.02	-3.0	0.01	0.7	0.6	73.5	-0.3	-34.5	-0.1	-11.6	**-11.6**	**30**
Sc	-8.7	-20.8	-19	-45.4	-6.8	-16.2	-13.8	-33	-8.6	-20.7	-22.7	-54.2	-5.6	-13.5	**-20.8**	**11.8**
V	-16.6	-13.8	-21.7	-18.1	-22.1	-18.5	1444.5	1206.4	27.1	22.7	-30.5	-25.5	-13.8	-11.5	**-13.8**	**182.8**
Cr	-327.4	-47.8	-398.6	-58.2	-268.8	-39.2	-271.8	-39.7	-193.8	-28.3	-383.7	-56	236.0	34.4	**-39.7**	**18.4**
Co	40.8	101.2	113.2	280.8	47.8	118.4	122.5	303.8	75.6	187.4	-1	-2.5	57.8	143.4	**143.4**	**79.3**
Ni	-68.2	-39.6	-90.8	-52.8	-56.5	-32.8	30.4	17.6	-12.9	-7.5	-79.5	-46.2	21.7	12.6	**-32.8**	**23**
Cu	-72.5	-60.6	1914.2	1599.1	2551.6	2131.6	76515.7	63919.6	4185.2	3496.2	-106.8	-89.2	-112.6	-94	**1599.1**	**9970.2**
Zn	62.5	288.5	35.2	162.3	90.9	419.2	980.9	4525.4	220.3	1016.2	42.2	194.7	71.7	330.8	**330.8**	**759.3**
Rb	-0.1	-90.8	-0.1	-97.2	-0.1	-82.3	-0.1	-81	0.02	22.1	0.0	-41.6	-0.1	-93.9	**-82.3**	**25.9**
Sr	-88.9	-63.9	-129.6	-93.1	-97	-69.7	-123.3	-88.6	-105.9	-76.1	-118.7	-85.3	-120.7	-86.8	**-85.3**	**8.4**
Y	0.3	7.1	1.6	36.3	0.3	6.2	-1.3	-29.8	-0.1	-1.5	0.2	4	2.2	51.3	**6.2**	**17.4**
Zr	-0.1	-2.3	4.2	129.2	1.5	45.5	1.6	51	-0.04	-1.2	-	-	5.8	179	**48.3**	**52.2**
Cs[1)]	-0.004	-87.5	-	-	-0.003	-68	-0.004	-79.4	-0.0001	-1.1	-0.004	-74.3	-	-	**-74.3**	**49.3**
Ba	-	-	-	-	0.7	31.3	-1.6	-71.6	7	317.2	1.2	52.7	-	-	**42**	**134**
La	0.3	168.6	-0.1	-50.9	0.0004	0.2	-0.1	-30.3	-0.05	-23.6	0.03	13.8	-0.1	-51.3	**-23.6**	**45**
Ce	1.1	173.2	-0.2	-28.5	0.01	1.4	-0.1	-17	-0.2	-25.8	0.4	58.5	-0.2	-35.3	**-17**	**46.1**
Pr	0.2	136.8	-0.04	-30.7	-0.003	-2.1	-0.05	-34.7	-0.1	-38.8	0.1	42.8	-0.02	-17.4	**-17.4**	**40.2**
Nd	0.8	90.2	-0.3	-33.1	-0.1	-9.8	-0.3	-35.8	-0.4	-38.5	0.2	25.6	-0.1	-11.7	**-11.7**	**30.5**
Sm	0.1	22.7	-0.1	-18.8	-0.05	-11.2	-0.1	-24.3	-0.1	-24.7	0.04	8.8	-0.02	-4.6	**-11.2**	**13.5**
Eu	-0.1	-24.3	-0.2	-63.0	-0.1	-48.5	-0.2	-80	-0.2	-60.2	-0.1	-34.3	-0.1	-46.7	**-48.5**	**14.0**
Gd	0.03	4.9	-0.1	-8.2	-0.03	-5.1	-0.1	-19.8	-0.1	-19.2	-0.1	-7.8	-0.0003	-0.05	**-7.8**	**6.7**
Tb	0.00002	0.01	-0.002	-1.8	-0.003	-2.7	-0.02	-14.2	-0.005	-4	-0.002	-1.4	0.002	1.5	**-1.8**	**3**
Dy	-0.02	-2.1	-0.02	-1.9	-0.02	-2.7	-0.1	-8.9	-0.03	-4.1	-0.1	-6.4	0.02	2.1	**-2.7**	**2.5**
Ho	-0.004	-2.1	-0.002	-1.2	-0.004	-2.5	-0.02	-8.7	0.002	1.1	-0.01	-6.3	0.002	0.9	**-2.1**	**2.6**
Er	-0.0001	0.0	0.01	1.5	-0.002	-0.4	-0.01	-2.2	0.02	3.5	-0.0001	-0.03	0.01	3	**-0.02**	**1.5**
Tm	0.002	2.5	0.003	4.7	0.001	0.9	0.003	4.1	0.0004	0.6	0.002	2.5	0.003	3.9	**2.5**	**1.2**

Yb	0.02	4.6	-0.01	-3	0.02	4	0.04	10.9	0.01	1.4	0.1	13	-0.001	-0.2	**4**	**4.3**
Lu	-0.002	-2.8	-0.0001	-0.2	0.0004	0.6	0.00	4.8	-0.001	-2.3	0.01	10.3	-0.01	-9.7	**-0.2**	**4.4**
Hf	-0.02	-10.9	0.03	18.4	0.03	17.1	0.1	39.7	-0.01	-8.4	0.8	513.8	0.1	96.9	**18.4**	**93.2**
Pb	-	-	-10.6	-98.1	-10.7	-99.1	-7.5	-69.6	-10.4	-96	-10.7	-99.2	-	-	**-98.1**	**114.5**
U	0.004	72.8	0.1	1058.9	0.03	533	10.3	181558.3	0.1	1819.6	0.01	167.5	0.004	70.1	**533**	**26303.8**
mass change term	1.6		2.3		1.3		1.0		1.5		2.7		1.2		**1.7**	
total mass change (%)															**-67.0**	

[1)] Cs is median value of Cs from layered gabbros in Wadi Tayin published in Peucker-Ehrenbrink et al., 2012

1185 **Table 3**

	Total flux Fault zone		Macquarie Island ophiolite[a)]	Composite section ODP[b)]
	median	range	range	
Major elements				
	10^{12}mol/year	10^{12}mol/year	10^{12}mol/year	10^{12}mol/year
Si	0.0540	-0.86 to 0.97	-1.17 to 0.33	2.78
Ti	-0.0386	-0.039 to -0.038	-0.25 to -0.08	0
Al	-0.1610	-0.79 to 0.47	-1.94 to 0.10	1.89
Fe	-0.1130	-0.24 to 0.013	-0.28 to 0.66	-
Mn	-0.0012	-0.0034 to 0.0011	-0.01 to 0.01	-
Mg	-0.503	-0.85 to -0.15	2.26 to 4.35	-2.75
Ca	-0.287	-0.569 to -0.0045	-5.48 to -4.16	1.68
Na	0.06	-0.047 to 0.17	1.79 to 2.81	1.49
H_2O	3.9400	2.75 to 5.13	17.6 to 19.8	17.6
Trace elements				
	10^{8} mol/year	10^{8} mol/year	10^{8} mol/year	10^{8} mol/year
Cu	-6.690	-41.9 to 28.9	-78 to -51	-
Zn	-1.400	-2.3 to -0.48	-12 to -1.0	-
Rb	-0.001	-0.004 to 0.002	- 1.2 to 2.2	0.77
Sr	13.0	7.48 to 18.4	- 7.1 to 22	11.00
Cs	-0.0003	-0.0003 to -0.0002	- 0.005 to 0.04	0.01
Ba	0.368	0.297 to 0.439	3.8 to 22	-
U	0.00045	-0.0007 to 0.002	-0.03 to -0.01	0.11

[a)] Coggon et al., 2016
[b)] After Staudigel (2014)

1186

List of Figures – with figure captions

Fig. 1: (a) Overview of the Samail ophiolite and (b) Wadi Tayin massif. Wadi Gideah is located approximately 20 km north of the town of Ibra. Map modified after (Nicolas et al., 2000).

Fig. 2: (a) Geological map of Wadi Gideah modified after (Peters et al., 2008). *Wadi Gideah cuts through a coherent series of oceanic crustal rock from the Moho transition zone up to the layered gabbros, foliated gabbros, high-level gabbros, and the sheeted dikes. The magmatic layering dips on average 28° S in the upper part of the valley. Approximately sub-orthogonal to the layering and steeply oriented chlorite-rich zones were mapped with a spacing of 1-2 km throughout the whole valley. The chlorite-rich fault zone investigated here is located about 1 km above the Moho. (b) Overview of the area around the chlorite-rich fault zone (displayed in yellow). Locations of fresh layered gabbro samples are shown in light grey squares and the location of the ICDP Oman Drilling Project Hole GT-1A is displayed with a pink triangle.*

Fig. 3: (a) Photo of the fault zone outcrop. Note a second chlorite-rich fault zone is located to the East. Especially in the hanging wall, the gabbros are intensely altered. (b) A detailed overview of the fault zone. Sample locations are marked; chlorite-rich fault zone (light blue diamonds), clasts (dark blue circles), hanging wall and footwall (royal blue triangles). The stereographic projection (dip direction/dip) shows the orientation of the fault zone relative to the orientation of the magmatic layering around the fault zone and the upper part of the valley as well as the orientation of sheeted dikes (Pallister, 1981). *(c) Blow-up and sketch of the shear sense indicating a normal fault by top to the left domino-type fracturing of the clasts.*

Fig. 4: Thin section photomicrographs of typical alteration pattern. (a) Background gabbro in plain-polarized light. Clinopyroxene is partially replaced by tremolite. Intact crystals show the

formation of secondary oxides and partial overgrow of microcrystalline alteration phases. Plagioclase is well preserved, the formation of chlorite is focussed to grain boundaries. Olivine is heavily fractured and serpentinized, partially decomposed into iddingsite and opaque oxides, cores are mostly preserved. (b) Same area in cross-polarized light, revealing the mostly anhedral granular structure of tremolite and polysynthetic twinning of plagioclase. Note the microcrystalline chlorite at grain boundaries of plagioclase. (c & d) Plain polarized micrograph and BSE image of typical alteration within the footwall following the same systematics as for the background gabbros but forming veinlets by dissolving the magmatic phases. Pervasive disaggregation of clinopyroxene is more advanced. (e) Prehnite-laumontite vein through heavily altered gabbro of the hanging wall, in cross-polarized light. The magmatic assemblage is almost entirely replaced by pervasive fracturing-initiated alteration. The rock is intensely crosscut by a dense network of veins. Secondary phases, e.g., prehnite are well crystallized and intergrown with laumontite. (f) BSE image, details of a late vein, euhedral prehnite associated with laumontite and calcite. pl – plagioclase, cpx – clinopyroxene, ol – olivine, tr – tremolite, chl – chlorite, prh – prehnite, lmt – laumontite, cal – calcite.

Fig. 5: Thin section micrographs of fault rock samples. (a) Chlorite-rich fault rock in plain polarized light showing concentrically zoned alteration pattern of semi-opaque to opaque phases. Note the solid Cu nuggets. (b) BSE micrograph of concentrically layered alteration revealing the complexity of zoning. (c) Major element composition along a profile from A to A'. Concentrically zoned phases show variable contents of CuO, FeO and SiO_2. Zones are numbered according to (b) No primary phases are preserved. (d) Chlorite replacing initial magmatic minerals completely but outlines of former mineral grains still visible (yellow dotted lines). Chlorite is associated with fine-grained granular (< 20 µm) titanite and epidote. (e) Euhedral epidote crystals precipitated directly out of a hydrothermal fluid into open space. Associated chlorite is clean and does not co-exist with granular titanite and epidote suggesting precipitation from hydrothermal fluid rather than replacement of primary minerals as shown in (d).

Fig. 6: (a) % Anorthite measured in feldspars from hanging wall and footwall samples vs MgO (wt.%) content. Compared to plagioclase composition of gabbros from modern ocean crust (Alt et al., 2010) *and plagioclase of layered gabbros elsewhere in the Wadi Tayin massife* (Pallister and Hopson, 1981)*. The dashed line represents the median value of % anorthite ($An_{82\pm2\%}$) measured in fresh layered gabbros of samples close to the fault zone outcrop (J. Koepke, unpublished data). High An-content of An_{91-95} measured in fresh plagioclase suggest very primitive compositions. (b) Compositions of amphiboles measured in hanging wall and footwall samples compared to amphibole composition measured in layered gabbros elsewhere in the ophiolite (Bosch et al., 2004) and in the plutonic section of modern oceanic crust at ODP/IODP Site 1256 (Alt et al., 2010). Note the high amount of tremolite pointing towards a formation regime of high Mg concentration. (c) Compositions of chlorite replacing plagioclase and chlorite-tremolite patches in between plagioclase and pyroxene grains (Fig.4b) measured in hanging wall and footwall samples in contrast to chlorite compositions of the fault rock. In comparison chlorite composition measured in upper and lower gabbros from Wadi Haymiliya in the central part of the ophiolite* (Nehlig and Juteau, 1988)*, chlorite measured in isotropic high-level gabbros in Wadi Gideah* (France et al., 2009) *and chlorite compositions measured in gabbros of modern oceanic crust at ODP/IODP Site 1256* (Alt et al., 2010)*.*

Fig. 7: Major- and trace element covariation diagrams for selected elements. Fault rock is shown in light blue diamonds, clast samples in dark blue circles, and hanging and footwall samples in royal blue triangles. Background layered gabbros are shown in grey squares and are from eight samples within a distance of 500 m to the fault zone outcrop. Open squares are olivine gabbro from elsewhere in Wadi Tayin (Peucker-Ehrenbrink et al., 2012)*. Green square represents the composition of chlorite measured in the fault rock and arrows indicate alteration vectors.*

Fig. 8: Chondrite-normalized REE for (a) background layered gabbros, (b) hanging wall and footwall, (c) clasts, and (d) chlorite-rich fault rock. The shaded grey area represents

chondrite-normalized REE of olivine gabbro observed elsewhere in the Wadi Tayin (Peucker-Ehrenbrink et al., 2012).

Fig. 9: $^{87}Sr/^{86}Sr$ vs Sr content (µg/g) of fresh layered gabbro within 500 m distance of the fault zone outcrop (grey squares), hanging and footwall samples (blue triangles), clast samples (dark blue dots), chlorite-rich fault rock (light blue diamonds), picked epidote from a epidote vein in the footwall (green cross), picked laumontite of a laumontite-calcite vein in the hanging wall (yellow star) and two picked calcite samples of a calcite vein within the fault rock and a calcite-laumontite vein in the hanging wall (orange crosses). Values of fresh layered gabbro of Wadi Tayin after Lanphere et al., (1981); McCulloch et al., (1981)*, Cretaceous seawater from* McArthur et al., (2001)*, modern groundwater sampled in gabbro hosted wells of Wadi Qafifah (personal communication N. Bompard) and values of Cretaceous to Miocene sediments from* Weyhenmeyer (2000).

Fig. 10: Major-and trace element gains and losses for all three rock types shown relative to the median value of fresh background layered gabbro (n=8). Elements are ranged by highest loss (left-hand side) to highest gain (right-hand side) plotted for the median fault rock. Note change in scale for gains greater than 100%.

Fig. 11: Schematic sketch showing the model set up of one fault zone (0.6 m of fault rock + 0.4 m of clasts with a total alteration halo of 30 m) in one block of lower crust (1 km x 1 km x 4 km). The ridge-parallel fault zone continues for 500 m and faults are spaced every 1 km perpendicular to the ridge axis.

Fig. 12: Hydrothermal fluxes (mol/y) extrapolated from estimated mass changes occurring during hydrothermal alteration in a lower crustal fault (green bars). In comparison hydrothermal fluxes calculated from pervasive hydrothermal background alteration for Macquarie Island ophiolite (white bars; Coggon et al., 2016) and a composite crustal section recovered by scientific ocean drilling (blue ovals; Staudigel, 2014). Diagram modified after

(Coggon et al., 2016). Fluxes for Ti, Mn, Cs, Ba and U are too small to be shown in this diagram.

Fig. 1

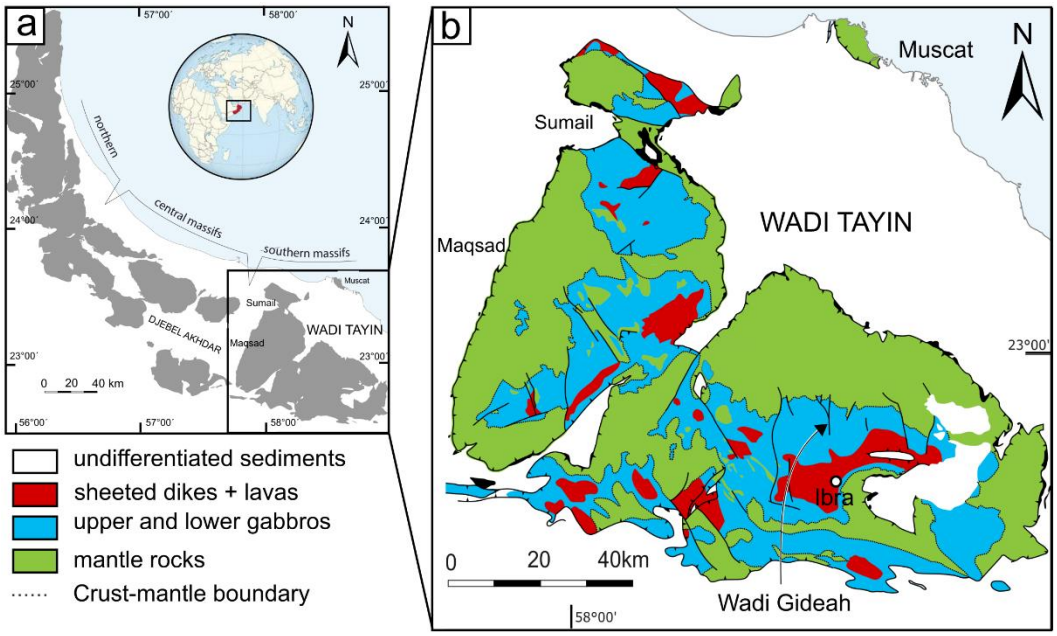

Fig. 2

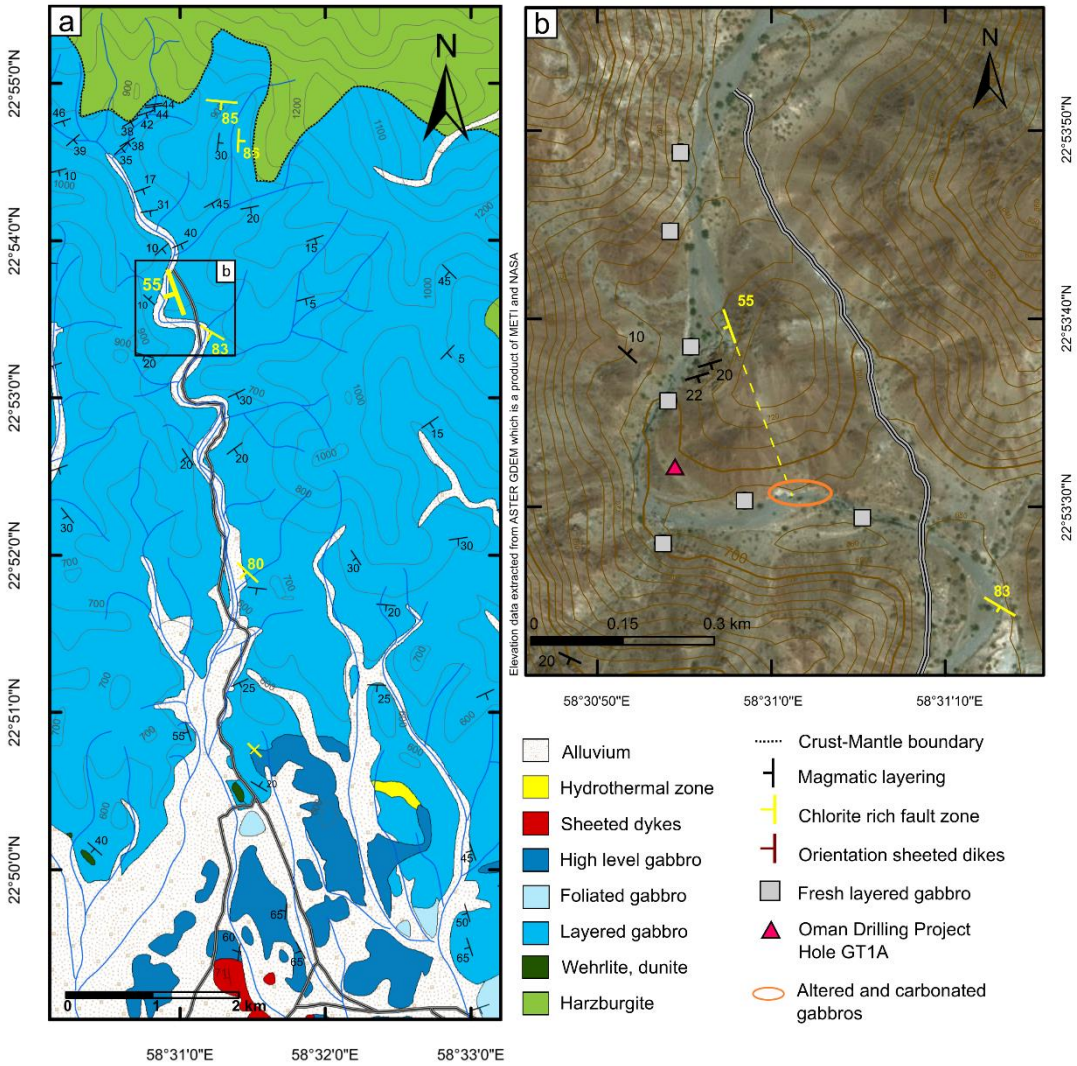
a
b
N
22°55'0"N
22°54'0"N
22°53'0"N
22°52'0"N
22°51'0"N
22°50'0"N
58°31'0"E
58°32'0"E
58°33'0"E
0
1
2km
Elevation data extracted from ASTER GDEM which is a product of METI and NASA
22°53'50"N
22°53'40"N
22°53'30"N
58°30'50"E
58°31'0"E
58°31'10"E
0
0.15
0.3 km
Alluvium
Hydrothermal zone
Sheeted dykes
High level gabbro
Foliated gabbro
Layered gabbro
Wehrlite, dunite
Harzburgite
Crust-Mantle boundary
Magmatic layering
Chlorite rich fault zone
Orientation sheeted dikes
Fresh layered gabbro
Oman Drilling Project Hole GT1A
Altered and carbonated gabbros

1318 **Fig. 3**

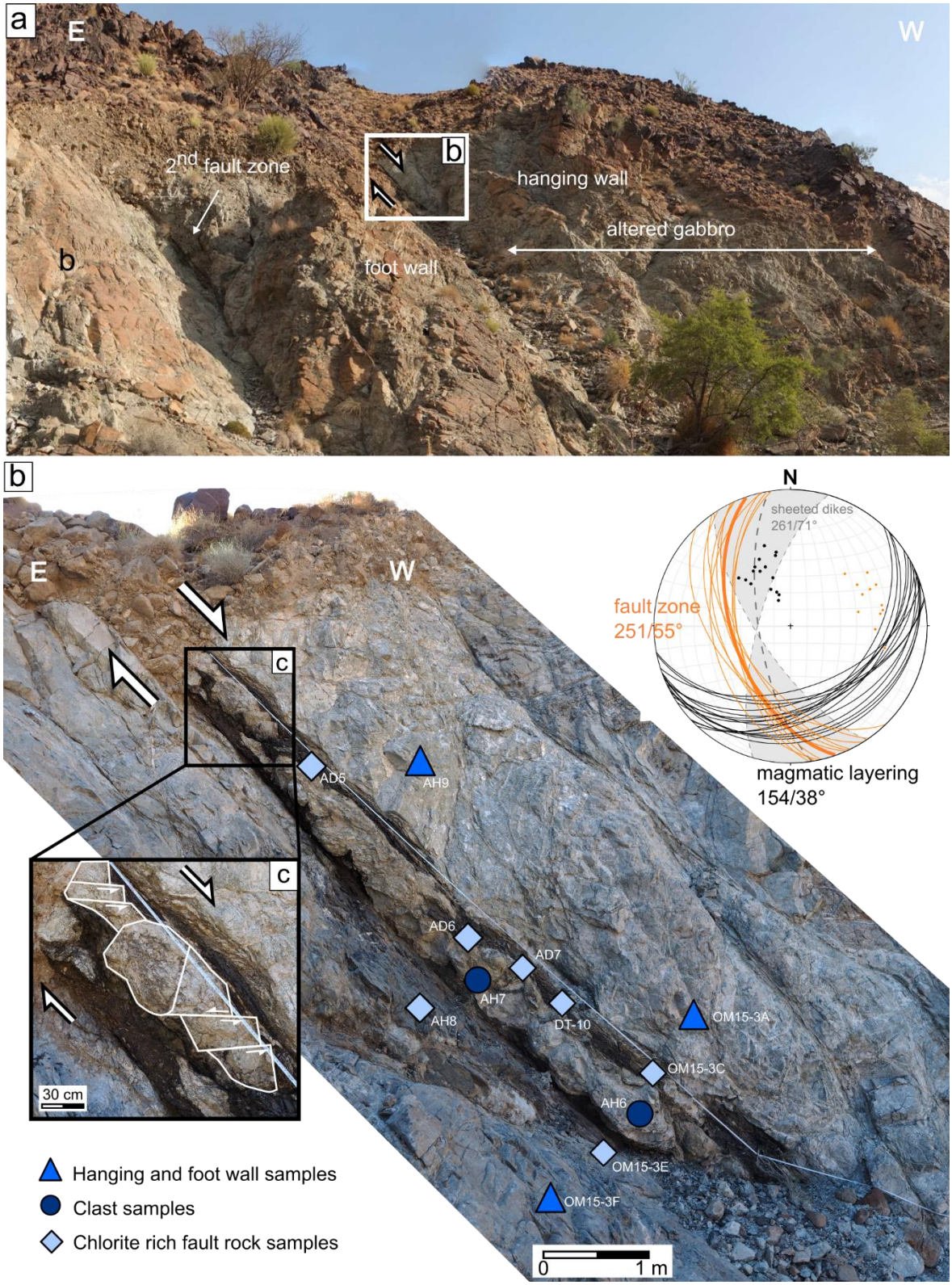

1319

1320

1321

Fig. 4

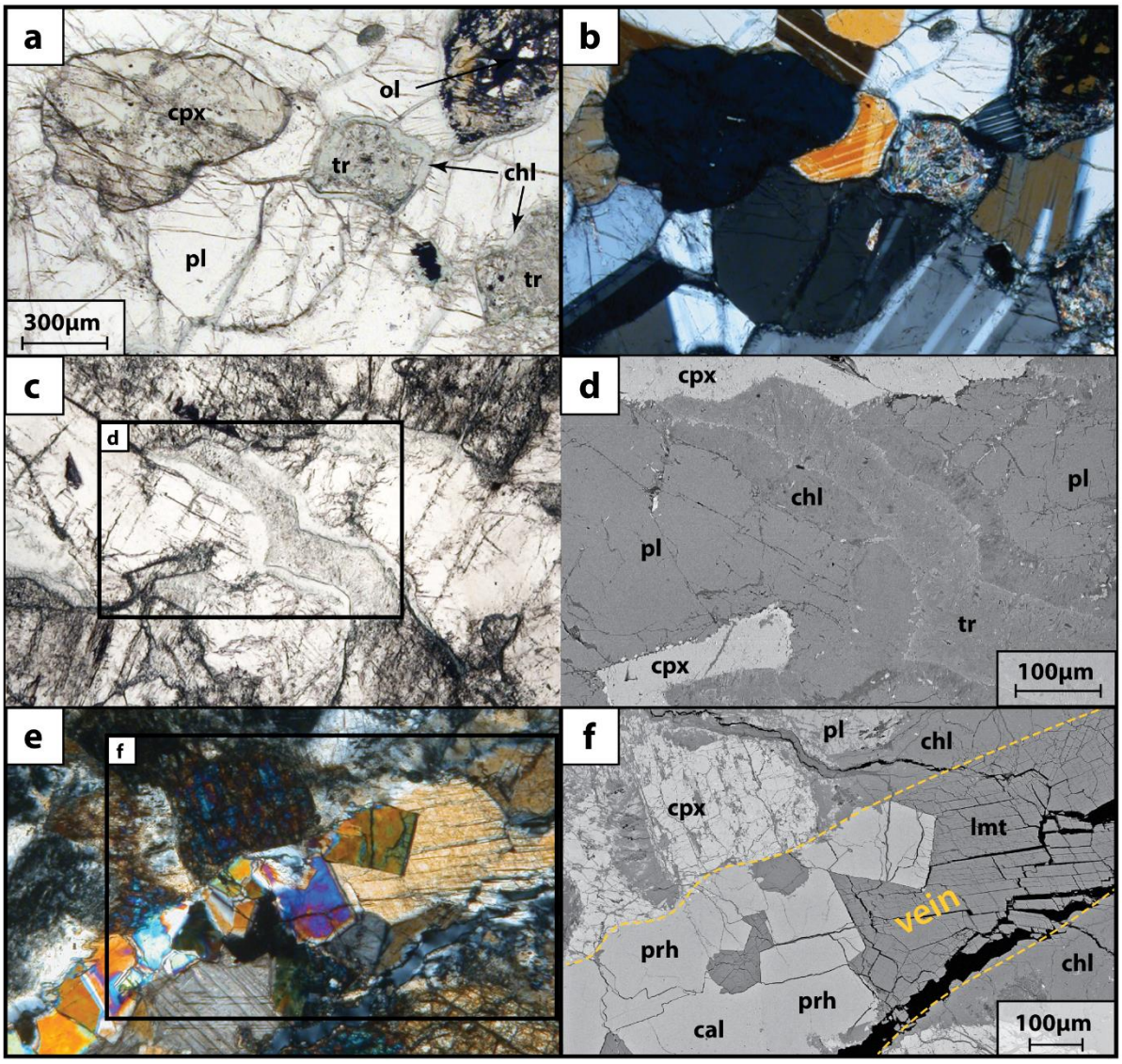
a
cpx
ol
tr
chl
pl
tr
300µm
b
c
d
d
cpx
chl
pl
pl
tr
cpx
100µm
e
f
f
pl
chl
cpx
lmt
vein
prh
chl
prh
cal
100µm

Fig. 5

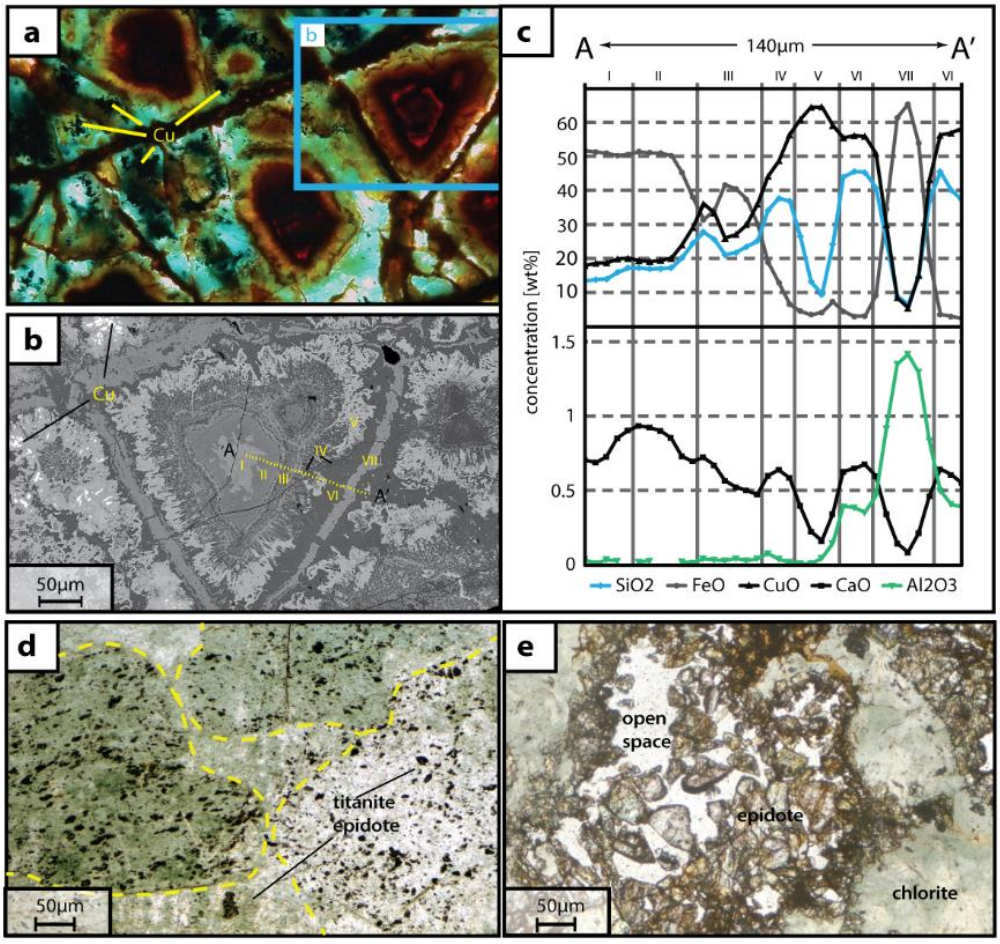
a
b
Cu
b
Cu
A
A'
I
II
III
IV
V
VI
VII
VIII
50µm
c
A
140µm
A'
I
II
III
IV
V
VI
VII
VI
60
50
40
30
20
10
concentration [wt%]
1.5
1
0.5
0
SiO2
FeO
CuO
CaO
Al2O3
d
titanite
epidote
50µm
e
open
space
epidote
chlorite
50µm

1342 **Fig. 6**

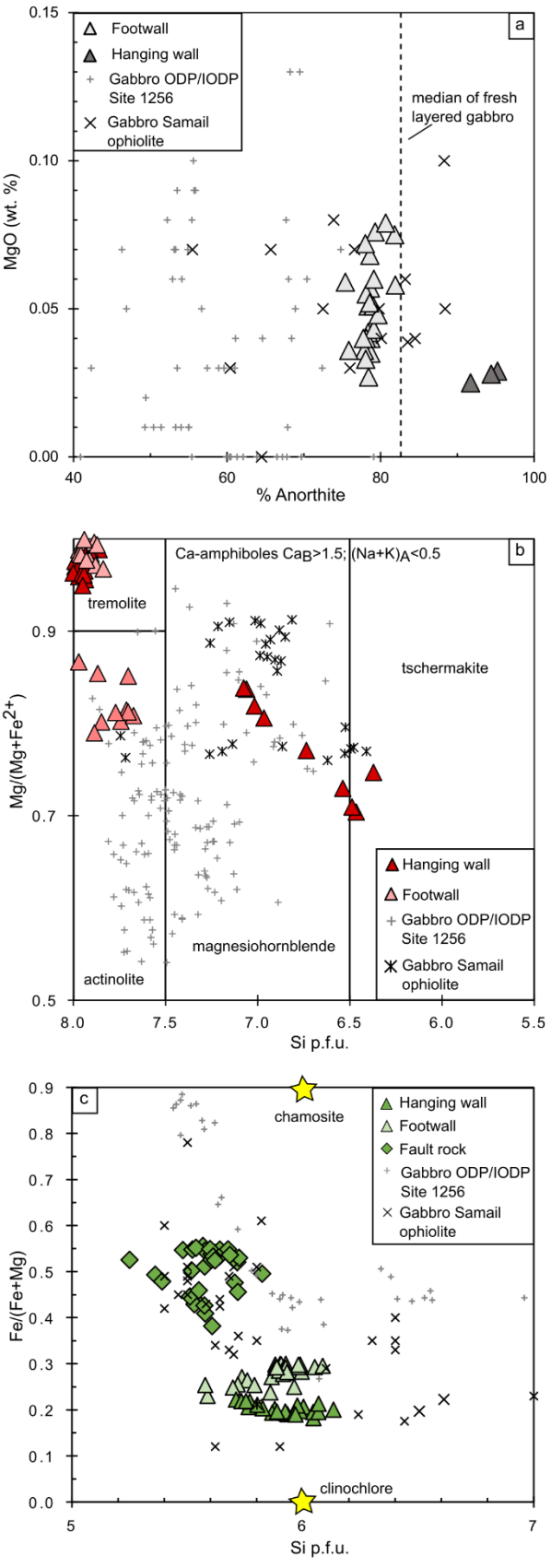

1343

1344

1345 **Fig. 7**

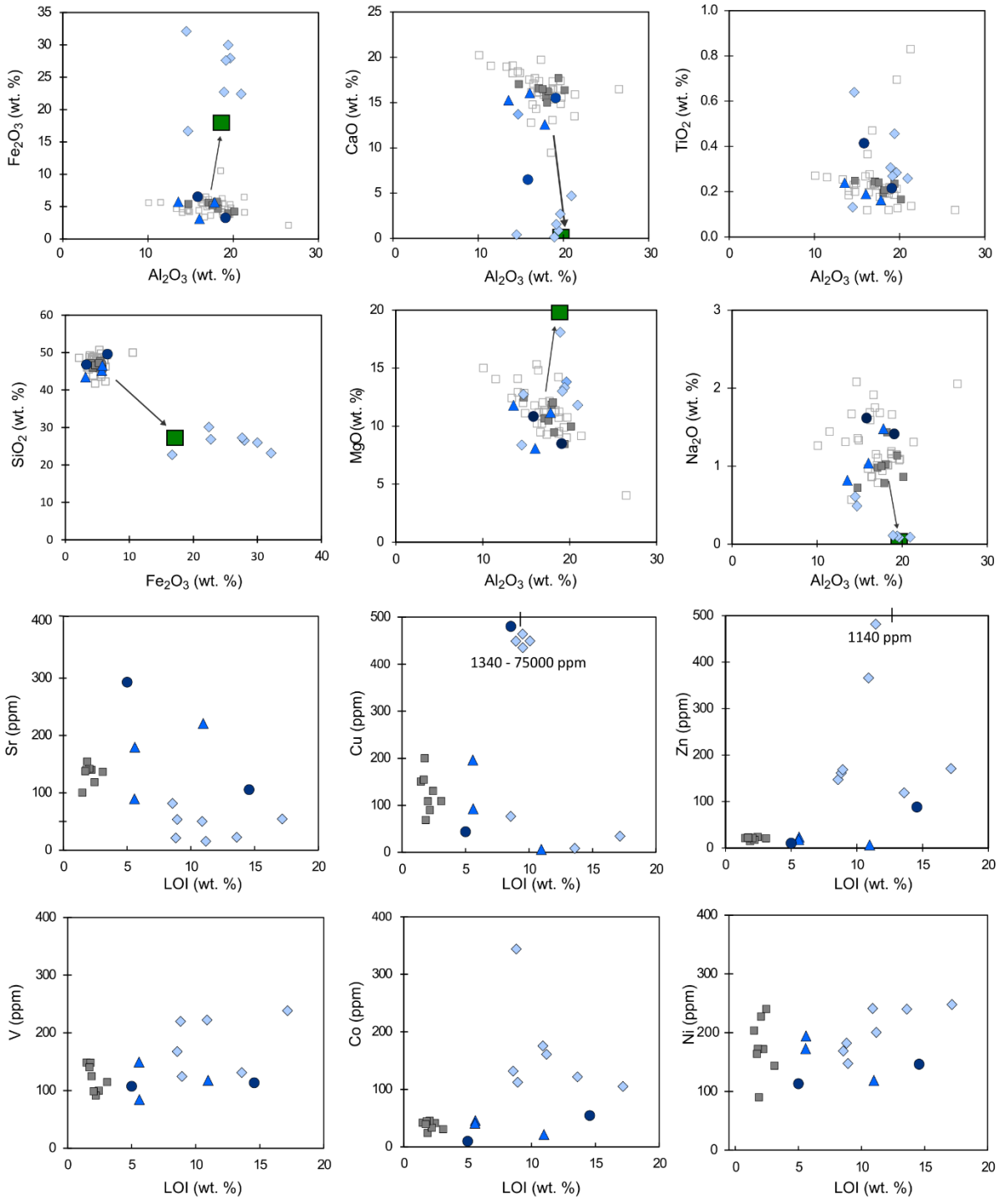

1346

1347

1348

1349

Fig. 8

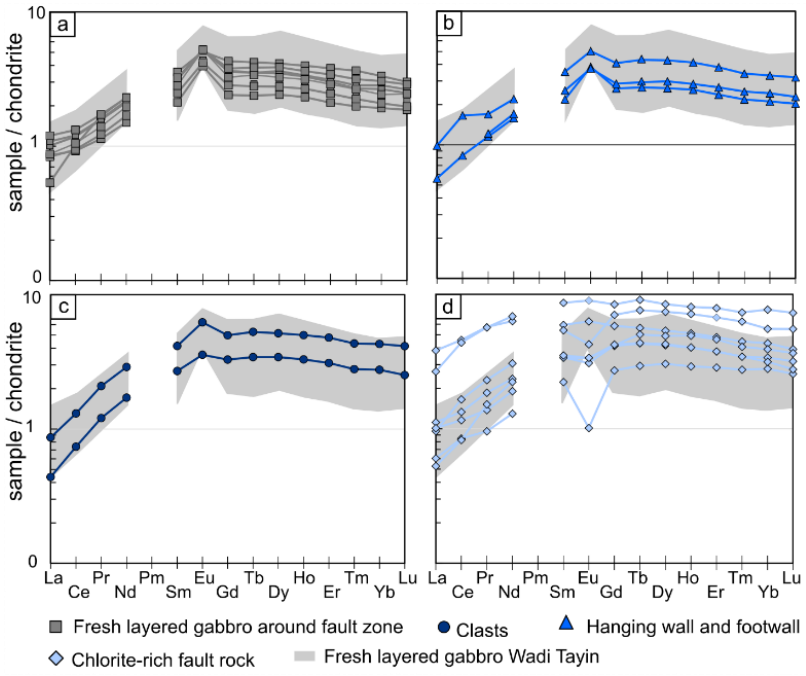
a
b
c
d
sample / chondrite
10
1
0
La Ce Pr Nd Pm Sm Eu Gd Tb Dy Ho Er Tm Yb Lu
Fresh layered gabbro around fault zone
Clasts
Hanging wall and footwall
Chlorite-rich fault rock
Fresh layered gabbro Wadi Tayin

Fig. 9

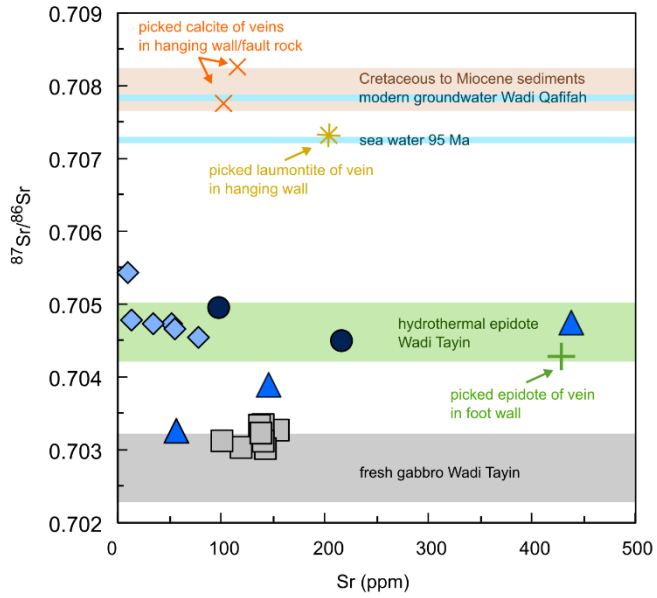
picked calcite of veins
in hanging wall/fault rock
Cretaceous to Miocene sediments
modern groundwater Wadi Qafifah
sea water 95 Ma
picked laumontite of vein
in hanging wall
hydrothermal epidote
Wadi Tayin
picked epidote of vein
in foot wall
fresh gabbro Wadi Tayin
87Sr/86Sr
0.709
0.708
0.707
0.706
0.705
0.704
0.703
0.702
0
100
200
300
400
500
Sr (ppm)

Fig. 10

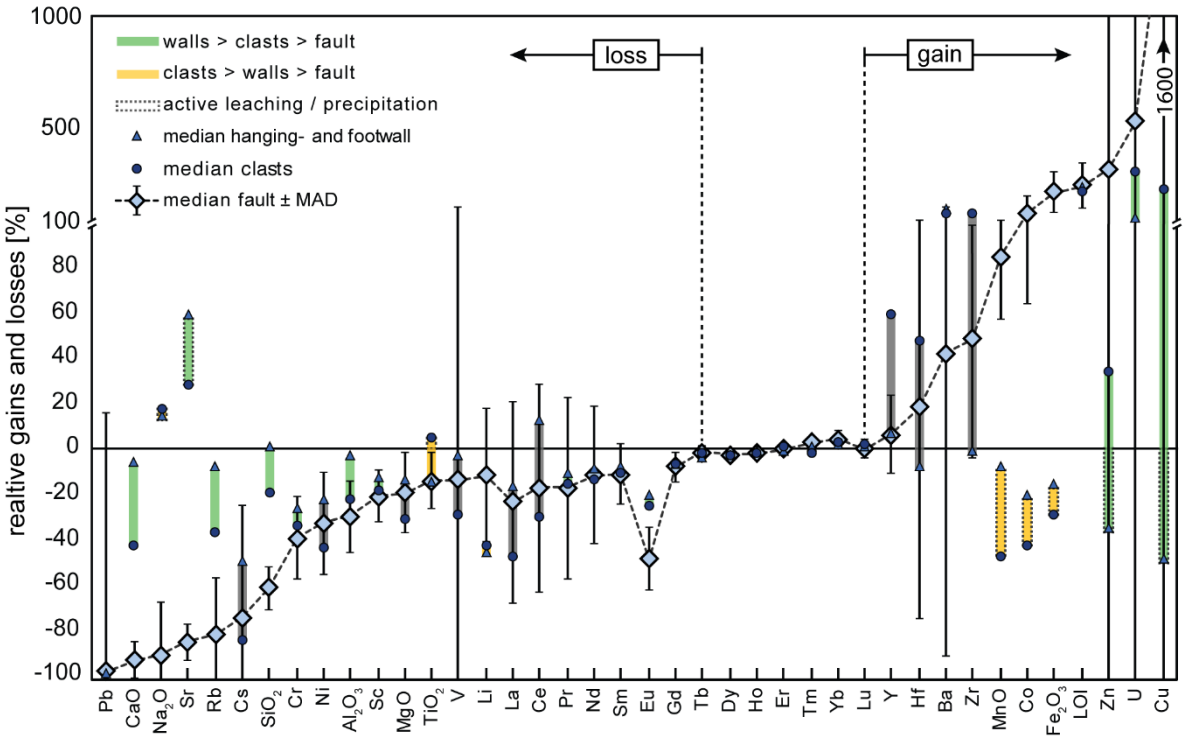
walls > clasts > fault
clasts > walls > fault
active leaching / precipitation
median hanging- and footwall
median clasts
median fault ± MAD
loss
gain
realtive gains and losses [%]
1000
500
100
80
60
40
20
0
-20
-40
-60
-80
-100
1600
Pb
CaO
Na2O
Sr
Rb
Cs
SiO2
Cr
Ni
Al2O3
Sc
MgO
TiO2
V
Li
La
Ce
Pr
Nd
Sm
Eu
Gd
Tb
Dy
Ho
Er
Tm
Yb
Lu
Y
Hf
Ba
Zr
MnO
Co
Fe2O3
LOI
Zn
U
Cu

Fig. 11

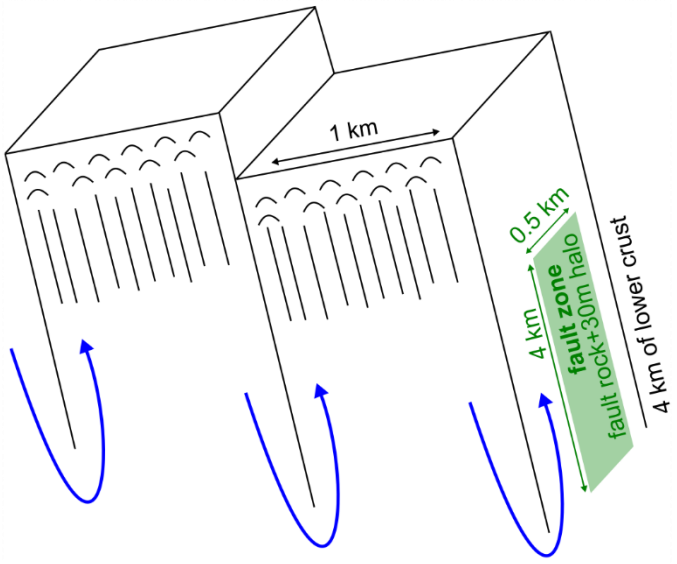
1 km
0.5 km
4 km
fault zone
fault rock+30m halo
4 km of lower crust

Fig. 12

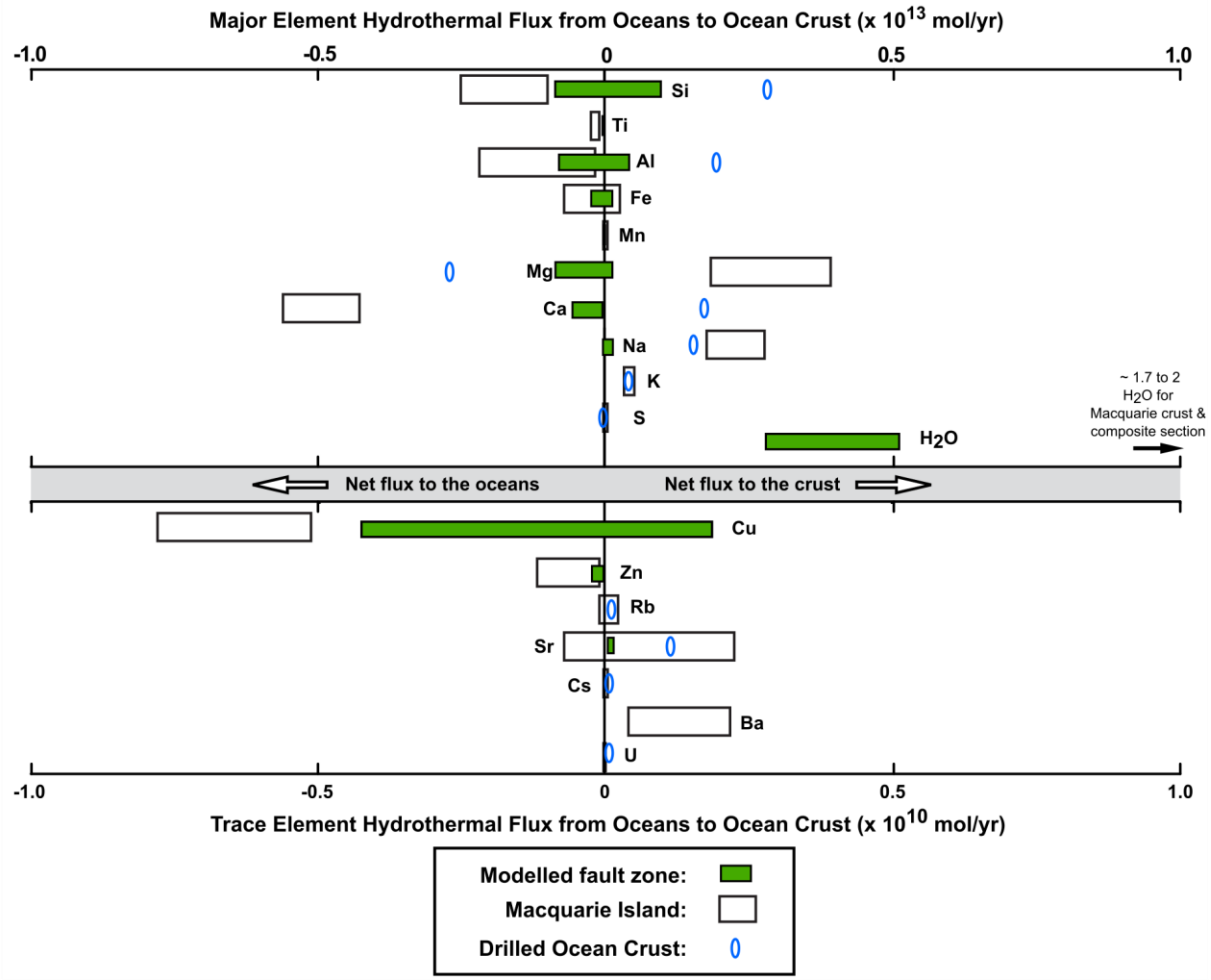

Supplementary materials

Table A1: Precision and accuracy of ICP-MS analysis from the University of Southampton and University of Hannover as well as precision and accuracy of XRF analysis from University of St. Andrews and University of Hamburg

Table A2: Composition of W. Gideah rock samples / background gabbros (major elements in wt%, ICP-OES data; trace elements in µg/g, ICP-MS data)

Table A3: EPMA data of plagioclase

Table A4: EPMA data of amphibole

Table A5: EPMA data of epidote

Table A6: EPMA data data of chlorite

Table A7: EPMA data of prehnite

Table A8: EPMA data of laumontite

A9: Supplementary figures